

Unified nuclear potential for heavy-ion elastic scattering, fusion, fission, and ground-state masses and deformations

H. J. Krappe

Hahn-Meitner-Institut für Kernforschung, Berlin, Germany

and Theoretical Division, Los Alamos Scientific Laboratory, University of California, Los Alamos, New Mexico 87545

J. R. Nix and A. J. Sierk

Theoretical Division, Los Alamos Scientific Laboratory, University of California, Los Alamos, New Mexico 87545

(Received 4 April 1979)

We develop a unified nuclear potential for the description of large-scale nuclear collective motion and find that it satisfactorily reproduces experimental data for heavy-ion elastic scattering, fusion, fission, and ground-state masses. Obtained by generalizing the modified liquid-drop model so that two semi-infinite slabs of constant-density nuclear matter have minimum energy at zero separation, this potential is given in terms of a double volume integral of a Yukawa-plus-exponential folding function. For heavy nuclear systems the resulting heavy-ion interaction potential is similar to the proximity potential of Swiatecki and co-workers. However, for light nuclear systems our potential lies slightly below the proximity potential at all nuclear separations. For heavy nuclei fission barriers calculated with our Yukawa-plus-exponential model are similar to those calculated with the liquid-drop model. However, for light nuclei the finite range of the nuclear force and the diffuse nuclear surface lower the fission barriers relative to those calculated with the liquid-drop model. Use of a Wigner term proportional to $|N - Z|/A$ in the nuclear mass formula resolves the major part of the anomaly between nuclear radii derived from elastic electron scattering on the one hand and from ground-state masses and fission-barrier heights on the other.

NUCLEAR REACTIONS ${}^4\text{He} + {}^{12}\text{C}$, ${}^{16}\text{O} + {}^{28}\text{Si}$, ${}^{84}\text{Kr} + {}^{208}\text{Pb}$; calculated heavy-ion interaction potential. ${}^{16}\text{O} + {}^{28}\text{Si}$, $E = 37.7, 81.0, 215.2$ MeV; calculated elastic-scattering angular distribution. ${}^{32}\text{S} + {}^{27}\text{Al}$, ${}^{35}\text{Cl} + {}^{62}\text{Ni}$, ${}^{16}\text{O} + {}^{208}\text{Pb}$; calculated compound-nucleus cross section. Calculated fission-barrier heights and ground-state masses for nuclei throughout Periodic Table. Nuclear potential energy of deformation, liquid-drop model, droplet model, modified liquid-drop model, Yukawa-plus-exponential model, proximity potential, Woods-Saxon potential, double-folding potential, optical model, ingoing-wave boundary condition, single-particle corrections, Strutinsky's method.

I. INTRODUCTION

For the description of large-scale nuclear collective motion, we may use either a microscopic approach or a macroscopic-microscopic approach. Within the former approach, substantial progress has been made recently in terms of the time-dependent mean-field (Hartree-Fock) approximation.^{1,2} However, even though possibly important effects such as collisions between particles are neglected,³⁻⁵ this method still requires a large amount of computing time to obtain predictions for specific cases.

In the latter approach, where smooth trends are obtained from a macroscopic model and local fluctuations are obtained from a microscopic model,⁶⁻⁸ the focus from the outset is on those collective degrees of freedom that are most relevant to the process under consideration. A complete dynamical theory requires the nuclear potential energy of deformation, the collective kinetic en-

ergy, and the dissipation function that specifies the conversion of collective energy into single-particle excitation energy. The major effort in this approach has been directed to calculating the local fluctuations in the potential energy by use of Strutinsky's method.⁶⁻⁸ However, the smooth trends in the potential energy are equally important, and it is with this aspect of the problem that we are concerned here.

The smooth part of the nuclear potential energy of deformation is often calculated by means of the liquid-drop model⁹ or the droplet model,¹⁰⁻¹² which are expansions of the nuclear energy in powers of $A^{-1/3}$ and $[(N - Z)/A]^2$. However, all such expansions break down for two nearly touching nuclei and for shapes with small necks. In these cases the finite range of the nuclear force and the diffuse nuclear surface lead to a reduction in energy that must be taken into account.

One way to incorporate the finite range of the nuclear force and the diffuse nuclear surface is

by means of a statistical calculation, such as with the Thomas-Fermi method^{10,13} or the energy-density formalism.¹⁴⁻¹⁸ By means of relatively simple statistical methods and phenomenological nucleon-nucleon potentials or energy-density functionals, a large number of average nuclear properties can be reproduced. However, for very deformed shapes a large amount of computing time is required.

A much simpler way is to calculate the smooth part of the nuclear energy by means of a double volume integral of a Yukawa function,¹⁹ in analogy with the calculation of the Coulomb energy by means of a double volume integral of the Coulomb interaction. This method has been used extensively,¹⁹⁻²³ but suffers from two related major deficiencies: First, the range $a = 1.4$ fm of the Yukawa function that is required to reproduce heavy-ion interaction-barrier heights is so large that the tail of the interaction potential extends to much larger distances than that determined from heavy-ion elastic scattering.^{24,25} Second, for two semi-infinite slabs of nuclear matter the resulting interaction potential does not have a minimum value when the slabs are in contact, as is required for a saturating nuclear system.

These two deficiencies can both be corrected by use of a folding function that contains *two* Yukawa functions.^{18,26,27} This introduces two additional parameters: another strength and another range. One of these parameters is eliminated by imposing the saturation condition, and the other is eliminated by taking the limit as the ranges of the two Yukawa functions approach each other, as is required by heavy-ion elastic-scattering data. The resulting folding function is the difference between an exponential and a Yukawa function, containing a single strength and a single range.

In Sec. II we derive a general expression for this Yukawa-plus-exponential potential, as well as specialized expressions for several geometrical shapes of interest. The form used for the nuclear mass formula is also given in this section. Having determined the constants of the Yukawa-plus-exponential potential in Sec. III, we apply it to heavy-ion elastic scattering and fusion in Sec. IV, to fission in Sec. V, and to ground-state masses and deformations in Sec. VI. Finally, some limitations of our potential are discussed in Sec. VII.

II. YUKAWA-PLUS-EXPONENTIAL POTENTIAL

In the original single-Yukawa modified liquid-drop model, the generalized nuclear surface energy is given by¹⁹⁻²³

$$E_n = E_Y(a, c_s) + \frac{2}{3} \frac{r_0}{a} c_s A, \quad (1)$$

where

$$E_Y(a, c_s) = - \frac{c_s}{8\pi^2 r_0^2 a^3} \int \int \frac{e^{-\sigma/a}}{\sigma} d^3r d^3r', \quad (2)$$

with

$$\vec{\sigma} = \vec{r} - \vec{r}'.$$

The double integration is over the volume of the nuclear configuration, whose magnitude is held fixed at $\frac{4}{3}\pi R_0^3$ as the nucleus deforms. The equivalent-sharp-surface radius R_0 of the spherical nucleus is related to the nuclear-radius constant r_0 by

$$R_0 = r_0 A^{1/3},$$

where A is the nuclear mass number. The quantity a is the range of the Yukawa folding function; in the limit $a \rightarrow 0$, Eq. (1) yields exactly the surface energy of the liquid-drop model. The dependence of the effective surface-energy constant c_s upon the relative neutron-proton excess

$$I = (N - Z)/A$$

is taken to be

$$c_s = a_s (1 - \kappa_s I^2), \quad (3)$$

where a_s is the surface-energy constant and κ_s is the surface-asymmetry constant. The last term in Eq. (1) cancels the volume-energy term that is present in the double volume integral of the Yukawa function.

When specialized to two semi-infinite slabs of nuclear matter, Eq. (2) yields for the nuclear interaction energy per unit area

$$\mathcal{E}_Y(a, c_s, s) = - \frac{c_s}{2\pi r_0^2} e^{-s/a},$$

where s is the distance between their inner surfaces. This result violates the requirement that for a saturating nuclear system the interaction energy per unit area be a minimum at $s = 0$.

This saturation condition can be satisfied by use of a folding function that is the difference between two Yukawa functions, for which the interaction energy per unit area for two semi-infinite distributions becomes

$$\mathcal{E}_n(s) = \mathcal{E}_Y(a_1, c_{s1}, s) - \mathcal{E}_Y(a_2, c_{s2}, s).$$

Imposing the saturation condition

$$\left. \frac{d\mathcal{E}_n(s)}{ds} \right|_{s=0} = 0 \quad (4)$$

gives the relationship

$$\frac{c_{s1}}{a_1} = \frac{c_{s2}}{a_2}.$$

Furthermore, the effective surface-energy constant is given by

$$c_s = c_{s_1} - c_{s_2}.$$

Solving these two equations yields

$$c_{s_1} = \frac{a_1}{a_1 - a_2} c_s$$

and

$$c_{s_2} = \frac{a_2}{a_1 - a_2} c_s.$$

The generalized nuclear surface energy then becomes

$$\begin{aligned} E_n &= E_Y(a_1, c_{s_1}) - E_Y(a_2, c_{s_2}) \\ &= \frac{a_1 E_Y(a_1, c_s) - a_2 E_Y(a_2, c_s)}{a_1 - a_2}. \end{aligned} \quad (5)$$

By varying the ranges a_1 and a_2 to reproduce the values of heavy-ion elastic-scattering potentials at the radii where they are determined experimentally, we find that the two ranges need to be approximately equal. The limit of Eq. (5) as $a_1 \rightarrow a_2 \equiv a$ is given by

$$E_n = \frac{\partial}{\partial a} [a E_Y(a, c_s)]. \quad (6)$$

Upon substituting Eq. (2) and differentiating, we are led to the general result

$$E_n = - \frac{c_s}{8\pi^2 r_0^2 a^3} \iint \left(\frac{\sigma}{a} - 2 \right) \frac{e^{-\sigma/a}}{\sigma} d^3 r d^3 r'. \quad (7)$$

$$\begin{aligned} E_n &= \frac{c_s}{4\pi r_0^2} \iiint \left\{ 2 - \left[\left(\frac{\sigma}{a} \right)^2 + 2 \frac{\sigma}{a} + 2 \right] e^{-\sigma/a} \right\} P(z) \left[P(z) - P(z') \cos \phi - \frac{dP(z)}{dz} (z - z') \right] \\ &\quad \times P(z') \left[P(z') - P(z) \cos \phi - \frac{dP(z')}{dz'} (z' - z) \right] \frac{dz dz' d\phi}{\sigma^4}, \end{aligned}$$

where the z and z' integrations extend from one end of the shape to the other and the ϕ integration extends from 0 to 2π . For an axially symmetric shape the distance σ is given by

$$\sigma = [P^2(z) + P^2(z') - 2P(z)P(z') \cos \phi + z^2 + z'^2 - 2zz']^{1/2}.$$

Explicit expressions for various simple configurations can be obtained either by integrating Eq. (7) directly or by applying Eq. (6) to the corresponding expression in the single-Yukawa model.¹⁹ This is now done for some of the more important geometrical shapes of interest.

For a single spherical nucleus, we find that

$$E_n^{(0)} = \left\{ 1 - 3 \left(\frac{a}{R_0} \right)^2 + \left(\frac{R_0}{a} + 1 \right) \left[2 + 3 \frac{a}{R_0} + 3 \left(\frac{a}{R_0} \right)^2 \right] e^{-2R_0/a} \right\} E_s^{(0)}, \quad (8)$$

where

$$E_s^{(0)} = c_s A^{2/3} \quad (9)$$

is the surface energy of the spherical nucleus.

[If comparing Eq. (8) with Eq. (3) of Ref. 27, note that the middle term in square brackets should be multiplied by $A^{2/3}$ there.] As expected, the lead-

[If comparing this formula with Eq. (2) of Ref. 27, note that the overall minus sign is missing there.]

The integral in Eq. (7) would be zero if the \vec{r} and \vec{r}' integrations were both extended over all space. It therefore does not contribute a volume term to the energy and does not require a volume-energy renormalization as does Eq. (1) for the original single-Yukawa model.¹⁹⁻²³ The saturation condition (4) is seen to be equivalent to the requirement that the kernel of the double volume integral does not give rise to a volume term.

A twofold application of the Gauss divergence theorem transforms Eq. (7) into the double surface integral^{19,23}

$$\begin{aligned} E_n &= - \frac{c_s}{8\pi^2 r_0^2} \oint \oint \left\{ 2 - \left[\left(\frac{\sigma}{a} \right)^2 + 2 \frac{\sigma}{a} + 2 \right] e^{-\sigma/a} \right\} \\ &\quad \times \frac{\vec{\sigma} \cdot d\vec{S} \vec{\sigma}' \cdot d\vec{S}'}{\sigma^4}. \end{aligned}$$

For an arbitrary shape, the generalized nuclear surface energy in the Yukawa-plus-exponential model can therefore be computed numerically by means of a fourfold integral. For an axially symmetric but otherwise arbitrary shape, one of the azimuthal integrations can be performed trivially. With the nuclear surface specified in cylindrical coordinates ρ, z, ϕ by the equation

$$\rho = P(z),$$

the resulting threefold integral is

ing term in Eq. (8) is the surface energy, which is proportional to $A^{2/3}$. The $A^{1/3}$ term, which represents the mean-curvature energy, is identically zero. The A^0 term and the exponentially small term arise from the finite range of the nuclear force and the diffuse nuclear surface.

We consider next the case of small distortions

about a spherical shape, with the nuclear surface specified in spherical coordinates r, θ, ϕ by the equation

$$r = R(\theta, \phi) = R_0 \left[1 + \sum_{n=0}^{\infty} \sum_{m=-n}^n \beta_{nm} Y_{nm}(\theta, \phi) \right].$$

In defining the spherical harmonic Y_{nm} , we use the phase convention of Edmonds.²⁹ The quantity β_{00} is determined in terms of the other coordinates by requiring that the volume remain constant; to first order it is zero. Similarly, the three quantities β_{1m} may be determined in terms of the other coordinates by requiring that the center of mass remain stationary, in which case they are also zero to first order. The generalized nuclear surface energy is then given to second order by

$$E_n = E_n^{(0)} + \frac{E_s^{(0)}}{4\pi} \sum_{n=2}^{\infty} C_n \sum_{m=-n}^n |\beta_{nm}|^2, \quad (10)$$

where

$$C_n = - \left[\left(\frac{R_0}{a} \right)^2 + 1 \right] + \left(\frac{R_0}{a} + 1 \right) \left[2 \left(\frac{R_0}{a} \right)^2 + \frac{R_0}{a} + 1 \right] e^{-2R_0/a} + 2R_0 \frac{\partial}{\partial a} \left[\left(\frac{R_0}{a} \right)^3 j_n \left(i \frac{R_0}{a} \right) h_n^{(1)} \left(i \frac{R_0}{a} \right) \right]. \quad (11)$$

Here j_n is the spherical Bessel function and $h_n^{(1)}$ is the spherical Hankel function of the first kind.³⁰ (Use of the same symbol n to denote nuclear energy and a summation index should cause no confusion.)

For the special case of small quadrupole distortions this result simplifies to

$$C_2 = 2 - 27 \left(\frac{a}{R_0} \right)^2 + \left[4 \left(\frac{R_0}{a} \right)^3 + 14 \left(\frac{R_0}{a} \right)^2 + 32 \frac{R_0}{a} + 52 + 54 \frac{a}{R_0} + 27 \left(\frac{a}{R_0} \right)^2 \right] e^{-2R_0/a}. \quad (12)$$

It is convenient to define the nuclear fissility parameter x as usual by³¹

$$x = \frac{E_C^{(0)}}{2E_s^{(0)}}, \quad (13)$$

where

$$E_C^{(0)} = \frac{3}{5} \frac{Z^2 e^2}{R_0} = a_c \frac{Z^2}{A^{1/3}} \quad (14)$$

is the direct Coulomb energy of the equivalent-sharp-surface spherical nucleus. The last step of Eq. (14) follows because the Coulomb-energy constant a_c is defined in terms of the nuclear-radius constant r_0 by

$$a_c = \frac{3}{5} \frac{e^2}{r_0}. \quad (15)$$

The critical value of x at which the spherical shape loses stability against fission is then

$$x_{\text{crit}} = \frac{1}{2} C_2, \quad (16)$$

which is less than unity for a nonzero value of a .

For two separated spherical nuclei of equivalent-sharp-surface radii R_1 and R_2 , we obtain

$$E_n = E_n^{(0)}(1) + E_n^{(0)}(2) + V_n,$$

where the nuclear interaction energy V_n may be written in the form

$$V_n = -D \left(F + \frac{s}{a} \right) \frac{R_{12}}{r} e^{-s/a}. \quad (17)$$

The distance s between the inner equivalent sharp surfaces of the two nuclei is given by

$$s = r - R_{12}, \quad (18)$$

where r is the distance between the centers of mass of the two nuclei, and

$$R_{12} = R_1 + R_2$$

is the sum of their equivalent-sharp-surface radii. The depth constant D is given by

$$D = \frac{4a^3 g(R_1/a) g(R_2/a) e^{-R_{12}/a}}{r_0^2 R_{12}} c'_s, \quad (19)$$

where

$$g(x) = x \cosh(x) - \sinh(x)$$

and, for the case of two separated nuclei,

$$c'_s = [c_s(1)c_s(2)]^{1/2}.$$

The constant F is given by

$$F = 4 + \frac{R_{12}}{a} - \frac{f(R_1/a)}{g(R_1/a)} - \frac{f(R_2/a)}{g(R_2/a)}, \quad (20)$$

where

$$f(x) = x^2 \sinh(x).$$

It should be stressed that Eq. (17) is valid only for $s \geq 0$. Determination of V_n for $s < 0$ would require specification of the physical process that occurs inside the contact point. We have not yet done this, but present instead in Sec. IV a simple quadratic parametrization of V_n that can be used for $s < 0$.

To facilitate comparisons with experimental data from various nuclear systems, it is often convenient to write V_n in an alternative form, which is motivated by noting that in the limit in which a is neglected compared to both R_1 and R_2 , the constant F approaches the value 2. Also, in the limit in which s is neglected compared to R_{12} , the quantity r/R_{12} approaches unity. We therefore write V_n in the reduced form

$$V_n/V_{\text{red}} = - \left(2 + \frac{s}{a}\right) e^{-s/a}, \quad (21)$$

where the potential reduction factor V_{red} is given *exactly* by

$$V_{\text{red}} = \frac{(F + s/a)R_{12}}{(2 + s/a)r} D, \quad (22)$$

which depends weakly on s .

If we neglect the exponentially small terms $\exp(-R_1/a)$ and $\exp(-R_2/a)$ compared to unity, then Eq. (22) simplifies to

$$V_{\text{red}} \approx \frac{a(R_1 - a)(R_2 - a) \left(4 - \frac{R_1}{R_1 - a} - \frac{R_2}{R_2 - a} + \frac{s}{a}\right) c'_s}{r_0^2(2 + s/a)r}. \quad (23)$$

Although it is in general *not* a good approximation to neglect the range a compared to both R_1 and R_2 and to neglect the separation s compared to R_{12} , we note for completeness that in this limit Eq. (23) simplifies further to

$$V_{\text{red}} \approx \frac{aR_1R_2c'_s}{r_0^2(R_1 + R_2)},$$

$$A_2 = a \frac{\partial}{\partial a} \left\{ \left[\frac{R_1}{a} \cosh\left(\frac{R_1}{a}\right) - \sinh\left(\frac{R_1}{a}\right) \right] \left\{ \left[\frac{a}{R_2} + 3 \left(\frac{a}{R_2}\right)^3 \right] \sinh\left(\frac{R_2}{a}\right) - 3 \left(\frac{a}{R_2}\right)^2 \cosh\left(\frac{R_2}{a}\right) \right\} \left[\frac{a}{r} + 3 \left(\frac{a}{r}\right)^2 + 3 \left(\frac{a}{r}\right)^3 \right] e^{-r/a} \right\}.$$

If both nuclei are deformed, then to first order Eq. (24) generalizes by the inclusion of an analogous term describing the deformation and orientation of nucleus 1.

To describe nuclear ground-state masses and deformations we augment our generalized nuclear surface energy E_n by a volume term (including a quadratic volume-asymmetry term),⁹ a Coulomb term (including surface-diffuseness^{11,12} and exchange³³ corrections), a Wigner term proportional to $|I|$,^{11,12} an electronic-binding-energy term,^{11,12} a pairing term,^{11,12} and a single-particle-correction term.^{9,11,12,34} The resulting macroscopic contribution to the mass excess of a spherical nucleus is then

$$M_{\text{macro}}^{(0)} = M_n N + M_H Z - a_v(1 - \kappa_v I^2)A + a_s(1 - \kappa_s I^2) \times \left\{ A^{2/3} - 3 \left(\frac{a}{r_0}\right)^2 + \left(\frac{r_0}{a} A^{1/3} + 1\right) \left[2A^{2/3} + 3 \frac{a}{r_0} A^{1/3} + 3 \left(\frac{a}{r_0}\right)^2 \right] e^{-2r_0 A^{1/3}/a} \right\} + \frac{3}{5} \frac{e^2}{r_0} \left[\frac{Z^2}{A^{1/3}} - \frac{5}{2} \left(\frac{b}{r_0}\right)^2 \frac{Z^2}{A} - \frac{5}{4} \left(\frac{3}{2\pi}\right)^{2/3} \frac{Z^{4/3}}{A^{1/3}} \right] + W(|I| + d) - a_{\text{el}} Z^{2.39} + \begin{cases} \Delta - \frac{1}{2}\delta & , N \text{ and } Z \text{ odd} \\ \frac{1}{2}\delta & , N \text{ or } Z \text{ odd} \\ -(\Delta - \frac{1}{2}\delta) & , N \text{ and } Z \text{ even} \end{cases} \quad (25)$$

where^{11,12,35,36}

$$\begin{aligned} M_n &= 8.071431 \text{ MeV}, \\ M_H &= 7.289034 \text{ MeV}, \\ e^2 &= 1.4399764 \text{ MeV fm}, \\ b &= 0.99 \text{ fm}, \end{aligned}$$

which agrees with the proximity theorem of Swiatecki and co-workers.³²

We consider now the generalization of Eq. (17) to the case in which a spherical nucleus 1 interacts with a deformed nucleus 2 whose nuclear surface is specified by

$$r = R_2 \left[1 + \sum_{n=0}^{\infty} \sum_{m=-n}^n \beta_{nm} Y_{nm}(\theta, \phi) \right]$$

in a coordinate system located at the center of mass of nucleus 2. In this same coordinate system, Θ and Φ denote the angular coordinates that specify the location of the center of mass of nucleus 1. Then to first order the nuclear interaction energy for this deformed configuration is given by

$$V_n^{\text{def}} = V_n - 4 \frac{R_2^3 c'_s}{a r_0^2} \sum_{n=2}^{\infty} A_n \sum_{m=-n}^n \beta_{nm} Y_{nm}(\Theta, \Phi), \quad (24)$$

where V_n is given by Eq. (17) and

$$A_n = -a \frac{\partial}{\partial a} \left[g\left(\frac{R_1}{a}\right) j_n\left(i \frac{R_2}{a}\right) h_n^{(1)}\left(i \frac{r}{a}\right) \right].$$

For the special case in which the deformation of nucleus 2 is of the quadrupole type, this result can be written explicitly as

$$\begin{aligned} W &= 30 \text{ MeV}, \\ a_{\text{el}} &= 1.433 \times 10^{-5} \text{ MeV}, \\ \Delta &= 12 \text{ MeV}/\sqrt{A}, \\ \delta &= 20 \text{ MeV}/A, \end{aligned}$$

and

$$d = \begin{cases} 1/A, & N \text{ and } Z \text{ odd and equal} \\ 0, & \text{otherwise.} \end{cases}$$

To obtain the total mass excess, we must add to Eq. (25) a correction arising from single-particle effects.^{9,11,12,34} If the ground-state shape is deformed, this single-particle correction includes also the changes in the Coulomb energy and generalized surface energy from their spherical values. To second order in deformation, this latter quantity is given by Eqs. (10) and (11).

III. DETERMINATION OF CONSTANTS

Four different types of experimental information are used to determine the values of the six constants r_0 , a , a_s , κ_s , a_v , and κ_v of our Yukawa-exponential model. These are elastic electron scattering, heavy-ion elastic scattering, fission-barrier heights, and ground-state masses. At this stage of our work, we take the strength W of the Wigner term and the pairing-energy parameters Δ and δ from Refs. 11 and 12.

Apart from elastic electron scattering, which determines the nuclear-radius constant r_0 , the experimental data do not determine the constants uniquely, but instead only relationships between two or more of them. In heavy-ion elastic scattering, this relationship is primarily between r_0 and a , but also involves a_s and κ_s weakly. In fission, the relationship is primarily between r_0 , a_s , and κ_s , but also involves a . In ground-state masses, the relationship involves all six constants that we adjust, as well as the coefficient W of the Wigner term. It is therefore important to proceed systematically, but somewhat iteratively, in the determination of the constants.

The nuclear-radius constant r_0 is related to the charge radius as determined from elastic electron scattering. Figure 1 shows experimental values of the equivalent-sharp-surface charge radius R divided by $A^{1/3}$, for a number of spherical nuclei throughout the Periodic Table. The original data were analyzed in terms of various functional forms for the charge distribution to extract values³⁷ of the root-mean-square charge radius $\langle r^2 \rangle^{1/2}$. We convert this root-mean-square radius into an equivalent-sharp-surface radius R by use of Fig. 2 of Ref. 38, under the assumption that the value^{11,12} of the constant b that characterizes the diffuseness of the surface is 0.99 fm.

However, we require the radius of the matter distribution as well as that of the charge distribution. Unfortunately, there is no model-independent way to infer a matter radius from a charge radius. Figure 1 also shows Myers' Thomas-

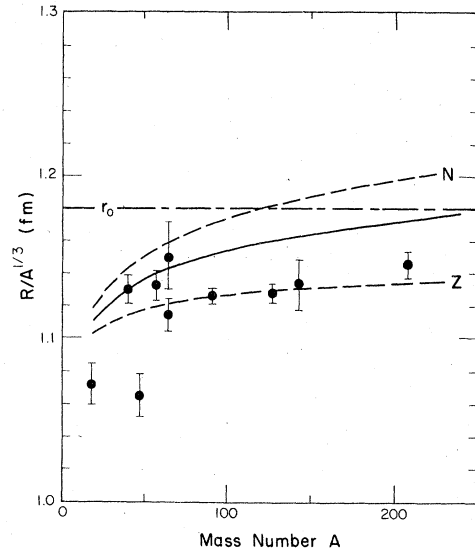


FIG. 1. Dependence upon mass number A of the equivalent sharp radius R divided by $A^{1/3}$. The experimental points give values of the charge radius for spherical nuclei, obtained from analyses of elastic-electron-scattering data (Ref. 37). These are to be compared with the lower dashed curve, which gives the result of a Thomas-Fermi calculation for the charge distribution (Refs. 11 and 12). The upper dashed curve and the solid curve give the corresponding calculated results for the neutron distribution and the total matter distribution, respectively. The dot-dashed curve indicates the value of 1.18 fm for the fundamental nuclear-radius constant r_0 that was used in these calculations.

Fermi calculation of the radii of the charge distribution, neutron distribution, and total matter distribution, for a value of the nuclear-radius constant $r_0 = 1.18$ fm, which had been adjusted to reproduce an earlier collection of charge radii.^{11,12} This particular Thomas-Fermi calculation yields a fairly large neutron skin, which thus far is neither confirmed nor ruled out by experimental data. As we go from heavy nuclei to light nuclei, the calculated neutron skin decreases because the neutron excess becomes smaller. Also, the calculated values of $R/A^{1/3}$ for the charge distribution, neutron distribution, and total matter distribution decrease because for light nuclei the surface tension is more effective in squeezing the nucleus and the Coulomb energy is less effective in dilating it than for heavy nuclei. For example, the calculated value of $R/A^{1/3}$ for the charge distribution is about 1.14 fm for heavy nuclei with $A \approx 250$, about 1.12 fm for medium-weight nuclei with $A \approx 100$, and about 1.10 fm for light nuclei with $A \approx 20$. Similarly, the calculated value of $R/A^{1/3}$ for the matter distribution is about 1.18 fm for heavy nuclei, about 1.15 fm for

medium-weight nuclei, and about 1.11 fm for light nuclei.

In a macroscopic theory of large-scale shape changes such as occur in fission and heavy-ion fusion, where the mass number A is discontinuous, it is extremely difficult to take into account the small changes in charge density and nuclear matter density that are implied by Fig. 1. If a single set of constants is required in a unified theory, we must select a value of $R/A^{1/3}$ that is independent of A . In principle, it would be possible to select one value of $R/A^{1/3}$ for the charge distribution and a slightly larger value for the matter distribution. The ultimate decision depends upon the relative weighting that is attached to the various types of experimental data that one plans to describe in terms of a single set of constants.

In our present considerations, we weight most heavily the use of our potential in calculating the most probable fission-fragment kinetic energy for the fission of a heavy nucleus, since conclusions concerning the mechanism of nuclear dissipation depend critically upon a correct calculation of this quantity. The calculated fission-fragment kinetic energy depends primarily upon the distance between the charge centers of the two fission fragments at the scission point. However, for charge distributions surrounded by a neutron skin, this distance is determined primarily by the radius of the matter distribution rather than that of the charge distribution. Although Fig. 1 would suggest that the density of the fissioning nucleus might be slightly larger at the scission point than at the ground state, other effects such as thermal expansion and charge polarization would increase the distance between charge centers at the scission point. For our present purposes, we therefore choose the value $r_0 = R/A^{1/3} = 1.18$ fm that corresponds to the matter distribution of heavy nuclei.

For medium-weight and light nuclei, radii calculated with $r_0 = 1.18$ fm are slightly larger than the experimental equivalent-sharp-surface radii. The range a that we determine from heavy-ion elastic scattering is therefore slightly smaller than it would have been had we instead used realistic radii. As will be seen in Sec. IV, for describing heavy-ion elastic scattering the values of r_0 and a are highly correlated. An inadequacy in our present choice of r_0 is therefore partially compensated by use of a slightly smaller range a . In future studies of heavy-ion elastic scattering, it might be preferable to use experimental equivalent-sharp-surface radii for the target and projectile, with the range a readjusted to a slightly larger value.

It is generally believed that heavy-ion elastic-

scattering data determine the real part of the optical potential in the vicinity of the strong-absorption radius.³⁹ This quantity is defined, for a given bombarding energy, as the distance of closest approach of a hypothetical Coulomb trajectory whose orbital angular momentum is such that the transmission probability for the optical potential barrier is $\frac{1}{2}$. For a given potential, the strong-absorption radius decreases with increasing bombarding energy.

To obtain experimental values for the real part of the optical potential at the strong-absorption radius, we use an optical-model analysis of elastic-scattering angular distributions for various systems at various bombarding energies.⁴⁰⁻⁴² The form factor for the real part of the optical potential used in this analysis is of the double-folding type, obtained by integrating the $M3Y$ short-range potential²⁶

$$v(\vec{r}) = \left(-262\delta(\vec{r}) + 7999 \frac{e^{-4r}}{4r} - 2134 \frac{e^{-2.5r}}{2.5r} \right) \text{ MeV} \quad (26)$$

over shell-model-generated density distributions for the target and projectile. [In Eq. (26) it is understood that distances are measured in units of fm.] The overall strength of the real potential, as well as in most cases the three parameters of a Woods-Saxon imaginary potential, were varied to optimally reproduce elastic-scattering data.

From this analysis, the value of the nuclear potential V_n at the strong-absorption radius is obtained for a variety of systems and energies. In order to eliminate the trivial dependence of the potential on the size of the nuclei, we express V_n in units of the reduction factor V_{red} defined by Eq. (22). Similarly, we convert the strong-absorption radius into the distance s between the inner equivalent sharp surfaces of the two nuclei by use of Eq. (18). When V_n/V_{red} is plotted versus s/a , then the experimental results for the various nuclear systems can be compared with the theoretical curve given by Eq. (21). Once $r_0 = 1.18$ fm has been specified, such a comparison can be used to determine the value of the range $a = 0.65$ fm to an accuracy of about 3%, as illustrated on a semi-logarithmic scale in Fig. 2. (The value of a determined in this way also depends weakly upon α_s and κ_s , whose values are determined later from comparisons with fission-barrier heights to be $\alpha_s = 21.7$ MeV and $\kappa_s = 3.0$.)

The significantly shorter range of 0.65 fm in the present Yukawa-plus-exponential model compared to 1.4 fm in the original single-Yukawa model¹⁹ arises from a combination of three effects: First, the functional form (17) of the pres-

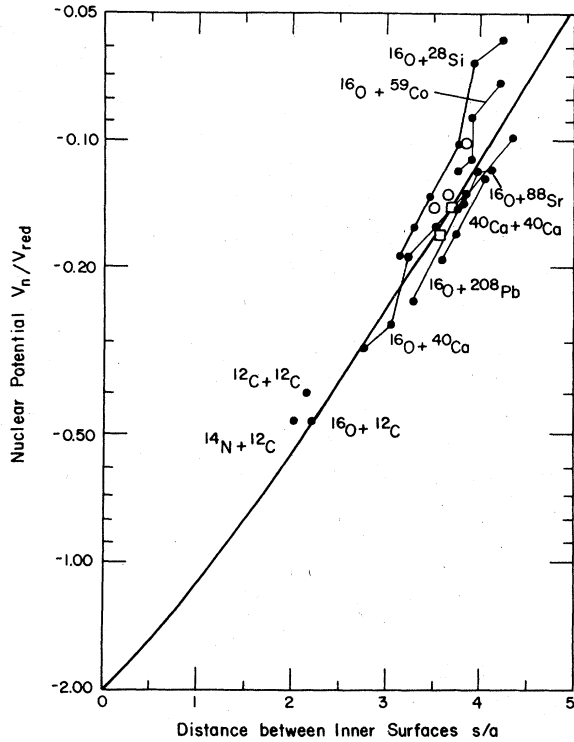


FIG. 2. Nuclear potential as a function of the distance between the inner equivalent sharp surfaces of two spherical nuclei. The potentials are plotted in units of the reduction factor V_{red} defined by Eq. (22), and the distance is measured in units of the range a of the folding function. The solid line is calculated from Eq. (21). The solid circles are obtained from optical-model analyses of heavy-ion angular distributions, with values for the same system at different bombarding energies connected by a thin solid line (Refs. 40–42). The open points are obtained from ingoing-wave-boundary-condition analyses of elastic-scattering excitation functions, with the open squares taken from Ref. 43 and the open circles taken from Ref. 44.

ent potential is different from that of the original potential. Second, the value of the nuclear-radius constant r_0 is now 1.18 fm, which is larger than the value of 1.16 fm that was used in the single-Yukawa potential. Third, we now use elastic-scattering data in the determination of the range, whereas in the original model only interaction-barrier heights and not their positions were used.

The analysis thus far has been based on the assumption that elastic scattering determines the potential near the strong-absorption radius within the context of an optical model. In order to check the sensitivity of the range to this specific interpretation of the optical model, we also include in Fig. 2 some data derived from interaction-barrier heights determined by ingoing-wave-

boundary-condition analyses, without the use of an imaginary potential.^{43,44} In these cases the experimental input data are elastic-scattering excitation functions in energy ranges close to the maxima in the interaction barriers. It is seen that these data follow the same trend as the optical-model data.

In appreciating the significance of variations in the experimental data in a semilogarithmic plot such as Fig. 2, we should note that the two upper points for $^{16}\text{O}+^{28}\text{Si}$, for which the values of V_n are -0.39 and -0.45 MeV, arise from the use of a previously determined imaginary potential, which leads to moderately large renormalizations of the $M3Y$ double-folding potential.^{40–42} Furthermore, the extracted values of the strong-absorption radii for these two points are larger than those for the other four points, although the laboratory energies of 141.5 and 215.2 MeV for these two points are higher than those for the other four points. Therefore, the propagation of experimental errors in the optical-model analysis becomes a very important question. Unfortunately, an error analysis analogous to that used in connection with the determination of charge distributions from electron scattering^{45,46} has never been made in a heavy-ion optical-model analysis.

Once r_0 and a have been specified, the surface-energy constant a_s and the surface-asymmetry constant κ_s are determined from comparisons with macroscopic contributions to fission-barrier heights for nuclei ranging from ^{250}Cm down to ^{179}Ta . The methods used to correct the experimental fission-barrier heights^{47,48} for single-particle effects^{34,49,50} are discussed in Sec. V. From this comparison the value of κ_s is determined to be 3.0 to an accuracy of about 17%. Once κ_s has been specified, the value of a_s is determined from fission-barrier heights to be 21.7 MeV to an accuracy of about 0.5%.

Of course, for fixed values of a and κ_s , the values of a_s and r_0 [or alternatively the Coulomb-energy constant a_C defined by Eq. (15)] that are required to reproduce experimental fission-barrier heights are highly correlated. Because a calculated macroscopic fission-barrier height depends primarily upon the value of the fissility parameter x defined by Eq. (13), experimental fission-barrier heights are reproduced almost equally well as long as

$$a_s = 29.637a_C. \quad (27)$$

This relationship is shown by the solid line in Fig. 3, with the solid circle indicating the particular values adopted here.

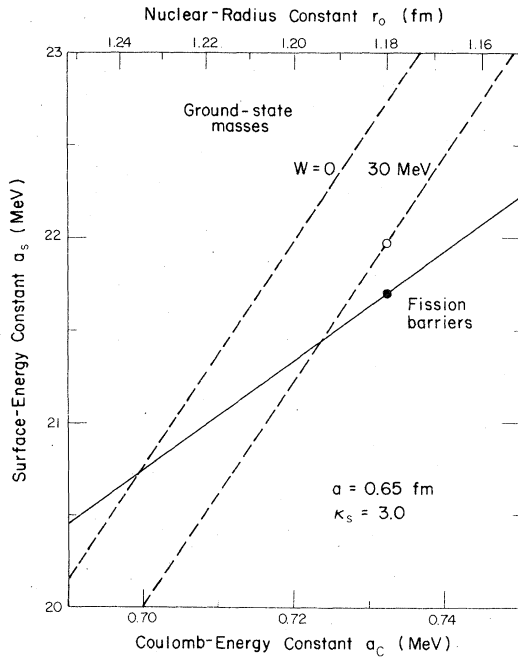


FIG. 3. Approximate relationships between the surface-energy constant a_s and the Coulomb-energy constant a_c (or alternatively the nuclear-radius constant r_0), for fixed values of the range a and the surface-asymmetry constant κ_s . The solid curve gives the relationship (27) determined from fission-barrier heights, with the solid circle indicating the values adopted here, corresponding to $r_0 = 1.18$ fm. The dashed curves give the relationship (28) determined from ground-state masses for the two indicated values of the Wigner coefficient W . The open circle indicates the values corresponding to $r_0 = 1.18$ fm and $W = 30$ MeV.

If, in addition to r_0 and a , the coefficient W of the Wigner term in the mass formula (25) were known, then the values of a_s and κ_s could also be determined in principle from experimental ground-state masses. As shown in Sec. VI, the resulting values of a_s and κ_s unfortunately depend somewhat upon the method that is used to correct the ground-state masses for single-particle effects and upon the sample of nuclei considered. When these corrections are calculated by use of the folded-Yukawa-II single-particle potential³⁴ for 165 even nuclei, and when $r_0 = 1.18$ fm, $a = 0.65$ fm, $W = 30$ MeV, and $\kappa_s = 3.0$, the resulting value of a_s determined from ground-state masses is 21.969 MeV. This value is shown by the open circle in Fig. 3.

The energy release in fission, which involves the difference between the ground-state masses of a heavy nucleus and two medium-weight nuclei, provides a relationship between a_s , a_c , and W ,

once a and κ_s have been specified. By keeping fixed the sum of the contributions from the surface, Coulomb, and Wigner energies to the energy release in the symmetric fission of ^{240}Pu , we obtain the simple result

$$a_s = 61.006a_c - 0.02512W - 21.946 \text{ MeV}. \quad (28)$$

The dashed lines in Fig. 3 give this result for two values of W .

It is seen that, within this approximate treatment, a mass formula without a Wigner term requires a radius parameter of $r_0 = 1.235$ fm to describe simultaneously ground-state masses and fission-barrier heights. That this radius parameter is inconsistent with elastic-electron-scattering data is a well-known anomaly in the liquid-drop model.⁹ The introduction of a Wigner term proportional to $|I|$, together with the important assumption that it is shape independent along the fission path between the ground state and the saddle point, permits the use of a smaller radius parameter. For example, with $W = 30$ MeV ground-state masses and fission-barrier heights would be reproduced simultaneously for $r_0 = 1.194$ fm, whereas with $W = 40.7$ MeV they would be reproduced simultaneously for $r_0 = 1.18$ fm.

We have not yet explored the effect that a larger value of W would have on the masses of light nuclei near the $N=Z$ line. Furthermore, there are other possible explanations of the nuclear-radius anomaly besides a Wigner term proportional to $|I|$. For example, the nuclear mass formula could require a shape-independent A^0 term of a different physical origin, such as the Gaussian-curvature energy.¹⁰ Although our Yukawa-plus-exponential model contains a Gaussian-curvature energy, whether it is realistic in magnitude and even sign is not known. Alternatively, it could require an A -dependent zero-point energy, which would be larger for light nuclei than for heavy nuclei. For these reasons, at this stage of our work we retain the value of 30 MeV determined by Myers^{11,12} and accept a slight reduction in the quality with which we are able to reproduce ground-state masses.

Once the values of all the other constants have been specified, the volume-energy constant a_v and the volume-asymmetry constant κ_v are determined from comparisons with experimental ground-state masses. As discussed in Sec. VI, these values depend slightly on the method that is used to correct for single-particle effects and upon the sample of nuclei considered. When single-particle corrections are calculated by means of Strutinsky's method from the folded-Yukawa-II single-particle potential,³⁴ a least-squares adjustment to the ground-state masses

of 165 even nuclei in the deformed actinide region and four regions of spherical nuclei throughout the Periodic Table yields the values $a_v = 16.012$ MeV and $\kappa_v = 2.04$.

The resulting complete list of values for the six constants of our Yukawa-plus-exponential model is therefore

$$r_0 = 1.18 \text{ fm}, \quad (29a)$$

$$a = 0.65 \text{ fm}, \quad (29b)$$

$$a_s = 21.7 \text{ MeV}, \quad (29c)$$

$$\kappa_s = 3.0, \quad (29d)$$

$$a_v = 16.012 \text{ MeV}, \quad (29e)$$

and

$$\kappa_v = 2.04. \quad (29f)$$

IV. HEAVY-ION ELASTIC SCATTERING AND FUSION

We now make more detailed comparisons of the predictions of our Yukawa-plus-exponential model with data from heavy-ion elastic scattering and fusion, which probe the nuclear potential at distances ranging from well beyond the contact point to slightly inside the contact point. At this time we do not consider inelastic scattering and nucleon-transfer reactions, but leave these applications of our model for the future.

The use of our Yukawa-plus-exponential potential as the real part of an optical potential requires some comment. We write the optical potential within the framework of Feshbach's theory as⁵¹

$$U_{op} = \left\langle \psi_0 \phi_0 \left| V + VQ \frac{1}{E - QHQ + i\epsilon} QV \right| \psi_0 \phi_0 \right\rangle, \quad (30)$$

where V and H are the potential and Hamiltonian for the entire system, ϵ is the averaging energy interval in the optical model, and $Q = 1 - P$, with P the projection operator on the elastic channel. The ground-state wave functions ψ_0 and ϕ_0 of the target and projectile are assumed to depend only on their internal coordinates, over which integration is implied by the brackets.

Satchler points out that if V arises from a realistic two-nucleon interaction (as in the $M3Y$ model), only the first term $\langle \psi_0 \phi_0 | V | \psi_0 \phi_0 \rangle$ is to be identified with a double-folding model.⁴¹ The second term in Eq. (30), reflecting the influence of all nonelastic channels on the elastic one, is in general complex, nonlocal, and energy dependent. Because of the Pauli exclusion principle, once the target and projectile overlap in ordinary space, the static polarization of their distribution functions in momentum space makes an important

contribution to the real part of the optical potential. This effect, together with the saturating properties of the interaction V , is supposed to be properly accounted for in our macroscopic model. We therefore expect that the static contribution of the second term of Eq. (30) to the real part of the optical potential is already included in our interaction potential (17).

In order to compare our Yukawa-plus-exponential potential with the $M3Y$ double-folding potential, we calculate the double-folding integral for the $M3Y$ potential (26) with Woods-Saxon density distributions rather than shell-model-generated density distributions.^{26,40-42} For the surface-diffuseness parameter of the Woods-Saxon density distribution we use the value 0.50 fm, and for the half-density radius C we use the result³²

$$C = R - \frac{b^2}{R}, \quad (31)$$

where

$$R = \left(1.28A^{1/3} - 0.76 + \frac{0.8}{A^{1/3}} \right) \text{ fm} \quad (32)$$

and

$$b = 1.0 \text{ fm}. \quad (33)$$

The folding integrals are evaluated conveniently in Fourier space, using the Fourier transform of the Woods-Saxon function given in Ref. 52. The resulting potential is compared in Figs. 4-6 with our Yukawa-plus-exponential potential for the light system ${}^4\text{He} + {}^{12}\text{C}$, the intermediate system

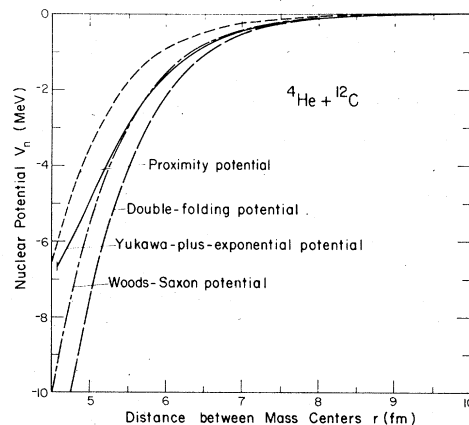


FIG. 4. Comparison of four nuclear potentials for the ${}^4\text{He} + {}^{12}\text{C}$ system. The Yukawa-plus-exponential potential is calculated by use of Eq. (17), which is valid only outside the contact point between the equivalent sharp surfaces, as indicated by the short vertical line. The proximity potential is obtained from Ref. 32, the double-folding potential is obtained from Ref. 26, and the Woods-Saxon potential is obtained from Ref. 53.

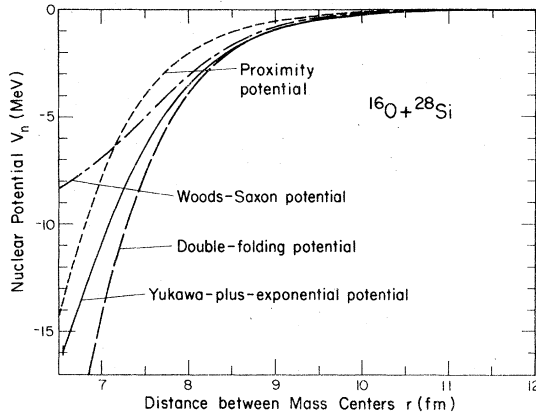


FIG. 5. Comparison of four nuclear potentials for the $^{16}\text{O} + ^{28}\text{Si}$ system. The proximity potential is obtained from Ref. 32, the double-folding potential is obtained from Ref. 26, and the Woods-Saxon potential is obtained from Rev. 54.

$^{16}\text{O} + ^{28}\text{Si}$, and the heavy system $^{84}\text{Kr} + ^{208}\text{Pb}$, respectively. For all three systems, the double-folding potential is significantly deeper than the Yukawa-plus-exponential potential near the contact point, but the two potentials are similar to each other near the strong-absorption radii.

We also show in Figs. 4–6 the cubic-exponential approximation to the proximity potential of Swiatecki and co-workers, which is given by³²

$$V_n(r) = \frac{b C_1 C_2 c'_s}{r_0^2 (C_1 + C_2)} \Phi \left[\frac{r - (C_1 + C_2)}{b} \right],$$

where in this case

$$c'_s = 17.9439 \left\{ 1 - 1.7826 \left[\frac{N_1 + N_2 - (Z_1 + Z_2)}{A_1 + A_2} \right]^2 \right\} \text{ MeV},$$

$$r_0 = 1.2249 \text{ fm},$$

and

$$\Phi(\xi) = \begin{cases} -\frac{1}{2}(\xi - 2.54)^2 - 0.0852(\xi - 2.54)^3, & \xi < 1.2511 \\ -3.437 \exp(-\xi/0.75), & \xi \geq 1.2511. \end{cases}$$

The quantities C_1 , C_2 , and b are obtained from Eqs. (31)–(33). For the heavy system, the proximity potential is very similar to our Yukawa-plus-exponential potential at all distances beyond the contact point. However, for the light and intermediate systems, the proximity potential is much weaker than our potential.

Part of the difference between the proximity potential and our Yukawa-plus-exponential potential arises because the equivalent-sharp-surface nuclear radii calculated by use of Eq. (32) in the former case are smaller than those calcu-

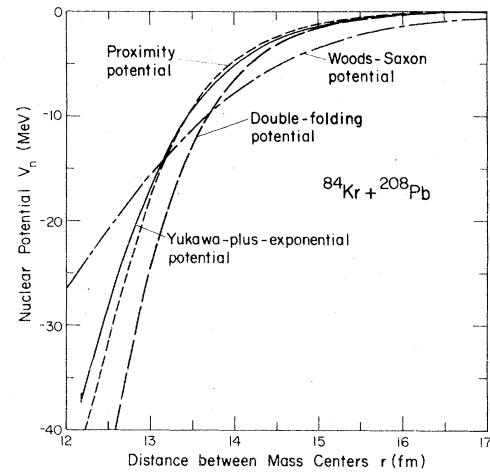


FIG. 6. Comparison of four nuclear potentials for the $^{84}\text{Kr} + ^{208}\text{Pb}$ system. The proximity potential is obtained from Ref. 32, the double-folding potential is obtained from Ref. 26, and the Woods-Saxon potential is obtained from Ref. 55.

lated with a nuclear-radius constant $r_0 = 1.18$ fm in the latter case. In particular, the sum of the equivalent-sharp-surface target and projectile radii is smaller in the proximity potential compared to the Yukawa-plus-exponential potential by 0.28 fm for the $^4\text{He} + ^{12}\text{C}$ system, 0.38 fm for the $^{16}\text{O} + ^{28}\text{Si}$ system, and 0.17 fm for the $^{84}\text{Kr} + ^{208}\text{Pb}$ system. Most of the remaining difference between these two potentials arises because near a common contact point, the proximity potential is deeper and has a shorter range compared to the Yukawa-plus-exponential potential.

For all three systems, the proximity potential is significantly weaker than the double-folding potential near and somewhat beyond the contact point, even though the equivalent-sharp-surface nuclear radii are in both cases calculated by use of the same Eq. (32).

Figure 4 also shows for $^4\text{He} + ^{12}\text{C}$ the real part of a Woods-Saxon optical potential determined⁵³ from an elastic-scattering angular distribution at a laboratory energy of 139 MeV. The similarity of this potential to our Yukawa-plus-exponential potential indicates that the latter can be used also for very light systems, without readjustments of the parameters. In Fig. 5 we also show for $^{16}\text{O} + ^{28}\text{Si}$ the real part of the E18 potential,⁵⁴ which is determined from a simultaneous adjustment to the forward-angle elastic-scattering angular distributions at laboratory energies of 37.7 and 215.2 MeV. Although this potential is rather shallow near the contact point, it agrees fairly well with the Yukawa-plus-exponential potential over a

wide range of distances near the strong-absorption radii.

The Woods-Saxon potential shown in Fig. 6 for $^{84}\text{Kr} + ^{208}\text{Pb}$ is determined⁵⁵ from the unresolved quasielastic angular distribution at a laboratory energy of 718 MeV. This potential intersects the other three potentials at a distance of approximately 13.2 fm, but lies well below the other potentials at larger distances.

The solid circles in Fig. 7 compare with our Yukawa-plus-exponential potential the experimental data analyzed by Christensen and Winther.⁵⁶ Their analyses are based on a critical distance that is slightly smaller than the distance of closest approach for a trajectory leading to the rainbow angle. Because of the very different quality of the experimental data used in Ref. 56, the scattering of the solid circles in Fig. 7 is easily understandable. For example, the three solid circles lying well above the curve between $s/a = 1.9$ and 2.5 correspond to very heavy systems, where the quasielastic scattering has not been resolved from the elastic scattering. The remaining solid points in Fig. 7 are derived from conventional optical-model analyses^{26, 54, 57, 58} and from an ingoing-wave-boundary-condition analy-

sis⁴³; the distances are taken to be the intersection points of various potentials that describe the elastic scattering equally well.

Figure 7 also shows values of the nuclear potential at the maximum in the interaction barrier, as derived from fusion excitation functions. These measurements probe the nuclear potential at distances closer to the contact point than do elastic-scattering measurements. The open circles are taken from a compilation by Birkelund and Huizenga,⁵⁹ which includes primarily measurements made by Scobel *et al.*⁶⁰ The open squares are taken from the work of David *et al.*⁶¹ The well-known uncertainty in deriving the barrier position from fusion excitation functions in a model-independent way gives rise to slanting error bars,⁵⁹ as illustrated in the figure for one point. Despite the absence of error analyses for the solid points derived from elastic scattering, substantial errors are associated with these points also.

Comparisons such as those in Fig. 7 may be regarded as attempts to extract a model-independent heavy-ion potential from elastic scattering and fusion. A more stringent test of our potential is to compare predicted angular distribu-

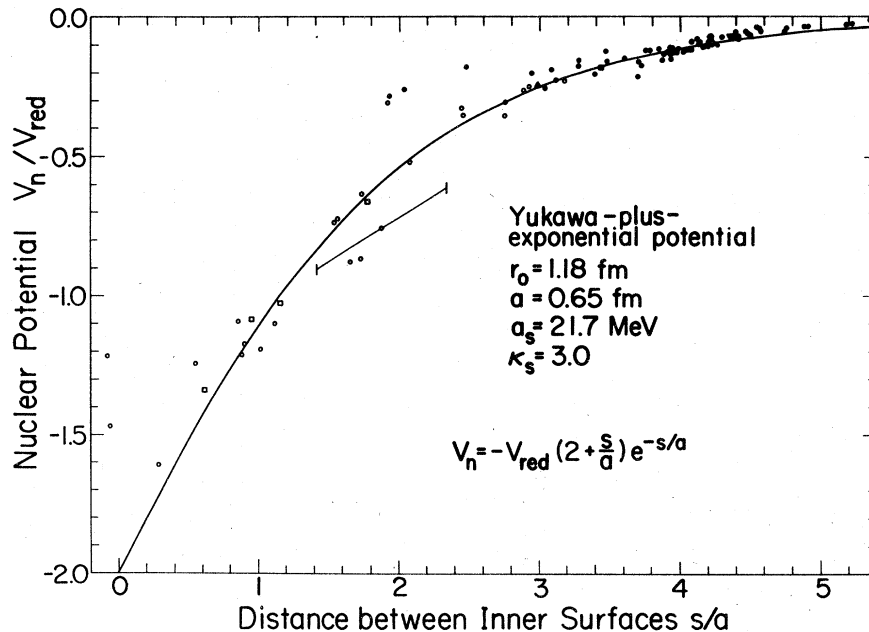


FIG. 7. Nuclear potential as a function of the distance between the inner equivalent sharp surfaces of two spherical nuclei. The potentials are plotted in units of the reduction factor V_{red} defined by Eq. (22), and the distance is measured in units of the range a of the folding function. The solid line is calculated from Eq. (21). The open points are obtained from heavy-ion fusion data, with typical uncertainties indicated by the error bar. The solid points are obtained from the values of heavy-ion elastic-scattering potentials at the radii where they are determined experimentally. The points are taken from the following: \circ from Refs. 59 and 60, \square from Ref. 61, \bullet from Ref. 56, \blacksquare from Ref. 57, \blacktriangle from Ref. 26, \blacktriangledown from Ref. 54, \blacklozenge from Ref. 43, and \bullet from Ref. 58.

tions and fusion excitation functions directly with experimental data. This is done in Fig. 8 for the elastic scattering of $^{16}\text{O} + ^{28}\text{Si}$ at laboratory energies of 37.7, 81.0, and 215.2 MeV.^{54, 62} (For the first case, we correct the incident energy of 38.0 MeV by 0.3 MeV to account for target energy loss, as suggested in Ref. 54. For the remaining two cases, corrections for target energy loss were made by the original investigators.)

For the real part of the optical potential we use Eq. (17) for distances outside the contact point defined by $r=R_{12}$. For distances inside the contact point we represent the potential by means of the parabola

$$V_r = -V_0 + B \frac{r}{R_{12}} + C \left(\frac{r}{R_{12}} \right)^2,$$

with B and C determined by requiring that the value of the potential and its first derivative be continuous at the contact point. This yields

$$B = 2V_0 - D \left[\left(\frac{R_{12}}{a} + 3 \right) F - \frac{R_{12}}{a} \right]$$

and

$$C = -V_0 + D \left[\left(\frac{R_{12}}{a} + 2 \right) F - \frac{R_{12}}{a} \right],$$

where D and F are defined by Eqs. (19) and (20).

The depth parameter V_0 depends upon the specific physical process that occurs inside the contact point. If the nuclei simply overlap with an increase in density in the overlap region, then V_0 could be determined within the frozen-density approximation³² by specifying the nuclear compressibility. If the nuclei instead change their shape so that the nuclear density remains roughly constant, then V_0 could be determined within the adiabatic approximation by specifying the sequence of shapes leading from the contact point to the compound system.²⁰ In the absence of other information to indicate the curvature of the potential inside the contact point, we may determine a representative value of V_0 by setting $C = 0$, corresponding to a linear extrapolation. For $^{16}\text{O} + ^{28}\text{Si}$ this yields $V_0 = 84.8$ MeV, which we use to calculate the results shown in Fig. 8 and Table I.

In calculating the Coulomb potential we take

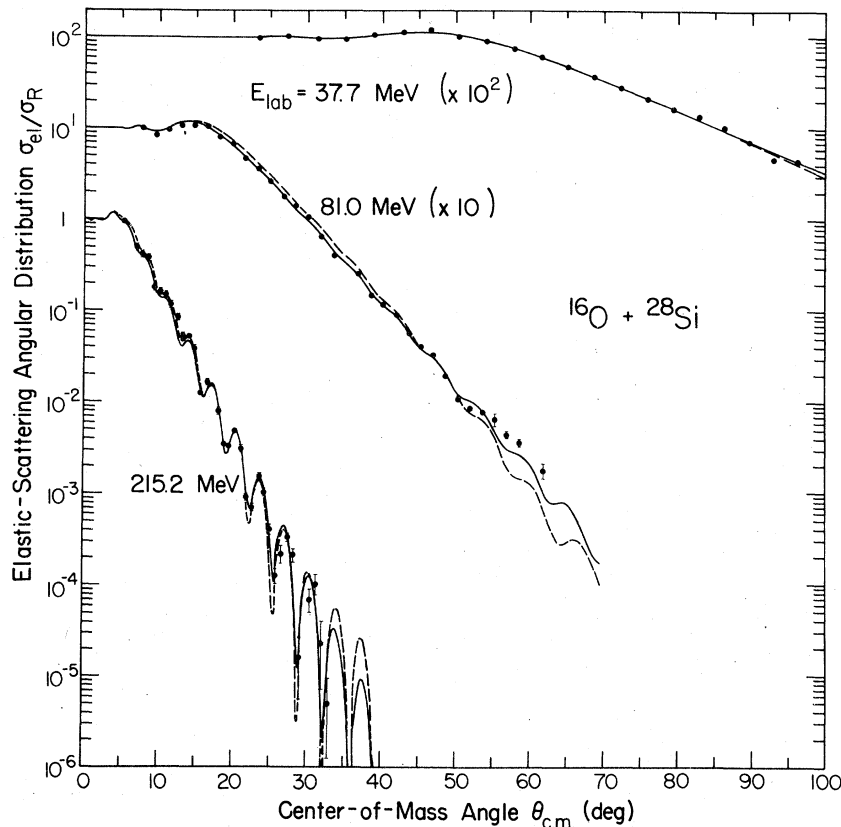


FIG. 8. Ratio of the elastic-scattering angular distribution to the Rutherford value for $^{16}\text{O} + ^{28}\text{Si}$ at three laboratory energies. The experimental points are taken from Refs. 54 and 62. The solid curves are calculated with our standard Yukawa-plus-exponential potential, and the dashed curves are calculated with the $E18$ potential of Ref. 54.

TABLE I. Parameters and χ^2/N of data points for the elastic scattering of $^{16}\text{O} + ^{28}\text{Si}$ at three laboratory energies. With the real potential given by our standard Yukawa-plus-exponential potential, the parameters W_0 , r_i , and a_i in a Woods-Saxon imaginary potential are varied to minimize χ^2/N . The sixth column gives the corresponding values of χ^2/N for the standard *E18* Woods-Saxon real and imaginary potentials of Ref. 54. The seventh column gives the values of χ^2/N that are obtained by varying five parameters in Woods-Saxon real and imaginary potentials, with the depth of the real potential held fixed at 10 MeV.

E_{lab} (MeV)	W_0 (MeV)	r_i (fm)	a_i (fm)	χ^2/N	χ_{E18}^2/N	$\chi_{5\text{-par}}^2/N$
37.7	207.28	1.060	0.492	1.5	1.2	1.2
81.0	32.95	1.157	0.680	2.5	9.5	2.4
215.2	18.55	1.238	0.717	5.3	4.9	4.6

into account the spatially extended diffuse charge distributions of the two ions in the same way as in Ref. 54. This approximate method consists of representing the Coulomb potential by the interaction of a point charge with a uniformly charged sphere of radius

$$R_C = r_C (A_1^{1/3} + A_2^{1/3}),$$

with

$$r_C = 1.0 \text{ fm}.$$

For the imaginary part of the optical potential, we use the Woods-Saxon potential

$$W(r) = -\frac{W_0}{1 + \exp[(r - R_i)/a_i]},$$

where

$$R_i = r_i (A_1^{1/3} + A_2^{1/3}).$$

The three parameters W_0 , r_i , and a_i are varied by use of the optical-model search program GENOA^{62, 63} to optimally reproduce the experimental angular distributions at each of the three laboratory energies. The resulting values of these parameters are given in Table I, along with the corresponding values of

$$\frac{\chi^2}{N} = \frac{1}{N} \sum_{i=1}^N \left(\frac{\sigma_i^{\text{exp}} - \sigma_i^{\text{calc}}}{\Delta_i} \right)^2,$$

where σ_i^{exp} and σ_i^{calc} are the experimental and calculated values of the cross section at the i th experimental point, Δ_i is the corresponding experimental error, and N is the number of experimental points.

We show for comparison in Table I the values of χ^2/N corresponding to the energy-independent

E18 potential of Ref. 54, as well as separate five-parameter adjustments in Woods-Saxon real and imaginary potentials, with a real well depth of 10 MeV. The results of the *E18* potential, which was adjusted simultaneously to the data at 37.7 and 215.2 MeV, are almost as good as the separate five-parameter results at these two energies, but are worse at the intermediate energy. The results of our standard Yukawa-plus-exponential real potential, with the three parameters of the imaginary potential varied, are slightly poorer at all three energies than the separate five-parameter results. The angular distributions calculated with the *E18* potential are compared with those calculated with the Yukawa-plus-exponential potential and with the experimental data in Fig. 8.

Because the values $r_0 = 1.18$ fm and $a = 0.65$ fm are determined from considerations other than the elastic scattering of $^{16}\text{O} + ^{28}\text{Si}$, the values of χ^2/N will decrease somewhat relative to those in Table I if these quantities are varied in addition to the three parameters of the imaginary Woods-Saxon potential. For the highest energy of 215.2 MeV, when r_0 is held fixed at 1.18 fm and a is varied, χ^2/N decreases from its original value of 5.3 at $a = 0.65$ fm to 5.1 at $a = 0.64$ fm. When a and r_0 are both varied, χ^2/N decreases to 4.8 at $r_0 = 1.12$ fm and $a = 0.73$ fm. For the two lowest energies of 37.7 and 81.0 MeV, the reduction in χ^2/N is much less when r_0 and a are varied.

The value of χ^2/N can also be reduced somewhat by varying the depth parameter V_0 that determines the potential inside the contact point, although the dependence of χ^2/N on V_0 is very complicated. For the highest energy of 215.2 MeV, when $r_0 = 1.18$ fm and $a = 0.65$ fm, there are at least three local minima in χ^2/N corresponding to different values of V_0 and the three parameters of the imaginary Woods-Saxon potential. These are $\chi^2/N = 4.2$ at $V_0 = 415$ MeV, $\chi^2/N = 4.6$ at $V_0 = 266$ MeV, and $\chi^2/N = 5.1$ at $V_0 \approx 0$, where the minimum is very flat. This demonstrates that for the highest energy of 215.2 MeV, elastic scattering is affected somewhat by the potential inside the contact point, since the potential outside the contact point is strictly independent of V_0 . For the two lowest energies of 37.7 and 81.0 MeV, the calculated results are nearly independent of V_0 .

For the highest energy of 215.2 MeV, we can reduce the value of χ^2/N even further by varying all parameters at our disposal, including a_s and r_C . In fact, there are at least two local minima with $\chi^2/N = 3.7$ and 3.8, corresponding to real potentials that never cross and that are roughly 15% different from each other at all distances outside the contact point. Given this situation, it

is clear that high-energy heavy-ion elastic scattering does not uniquely determine the real potential at the strong-absorption radius.

Although our Yukawa-plus-exponential potential satisfactorily reproduces the measured elastic-scattering angular distributions for $^{16}\text{O} + ^{28}\text{Si}$ at forward angles, it does not yield the pronounced backward-angle oscillations observed in this system at a laboratory energy of 55 MeV.⁶⁴

We have also applied our Yukawa-plus-exponential potential to the elastic scattering of other systems. For $^{12}\text{C} + ^{28}\text{Si}$, it reproduces the measured angular distributions^{62, 65} at laboratory energies of 24.0 and 186.4 MeV in a manner similar to that for $^{16}\text{O} + ^{28}\text{Si}$. The results for $^{12}\text{C} + ^{28}\text{Si}$ are also relatively insensitive to the value of V_0 , which determines the potential inside the contact point.

However, for $^6\text{Li} + ^{28}\text{Si}$ at a laboratory energy of 135.1 MeV, where rainbow scattering is observed,^{62, 65} the potential inside the contact point is very important. When our standard Yukawa-plus-exponential potential is used outside the contact point, χ^2/N has a sharp minimum of 3.5 at $V_0 = 200$ MeV, which is much larger than the value of 46 MeV obtained by setting $C = 0$ in a linear extrapolation. The corresponding value of χ^2/N for the *R22* Woods-Saxon potential of Ref. 65 is 2.6. As observed previously,⁶⁵ high-energy light-ion scattering is very different from heavy-ion scattering.

Excitation functions for compound-nucleus formation at energies close to the maximum in the interaction barrier are usually analyzed in terms of the result

$$\sigma_c(E) = \frac{\pi}{k^2} \sum_{l=0}^{\infty} (2l+1) P_l(E), \quad (34)$$

where E is the center-of-mass energy, k is the wave number at infinity, and $P_l(E)$ is the transmission coefficient for the l th partial wave, which is usually approximated by the Hill-Wheeler parabolic-barrier result⁶⁶

$$P_l(E) = \frac{1}{1 + \exp[2\pi(V_l - E)/(\hbar\omega_l)]}.$$

The quantity V_l is the height of the effective potential for the l th partial wave,

$$V(l, r) = V_n(r) + \frac{Z_1 Z_2 e^2}{r} + \frac{l(l+1)\hbar^2}{2\mu r^2},$$

where μ is the reduced mass. The curvature parameter ω_l is given by

$$\omega_l = \left[-\frac{\partial^2 V(l, r)}{\partial r^2} \right]_{r_i}^{1/2},$$

where r_i is the position of the maximum in $V(l, r)$. As discussed in Ref. 67, the Hill-Wheeler approximation for the one-dimensional transmission coefficients is sufficiently accurate provided that the dependences of V_l and ω_l on angular momentum are taken into account properly.

With $V_n(r)$ given by Eq. (17), we evaluate Eq. (34) for $\sigma_c(E)$ for three systems for which there are accurate measurements of the excitation functions for compound-nucleus formation.^{60, 68-70} As shown in Fig. 9, the calculated cross sections lie slightly below the experimental ones, with the discrepancy increasing as we go to heavier systems. This could arise because the barriers calculated with the Yukawa-plus-exponential potential are slightly too high, especially for heavier systems. Alternatively, a one-dimensional treatment in terms of the frozen-density approximation³² could be inadequate.

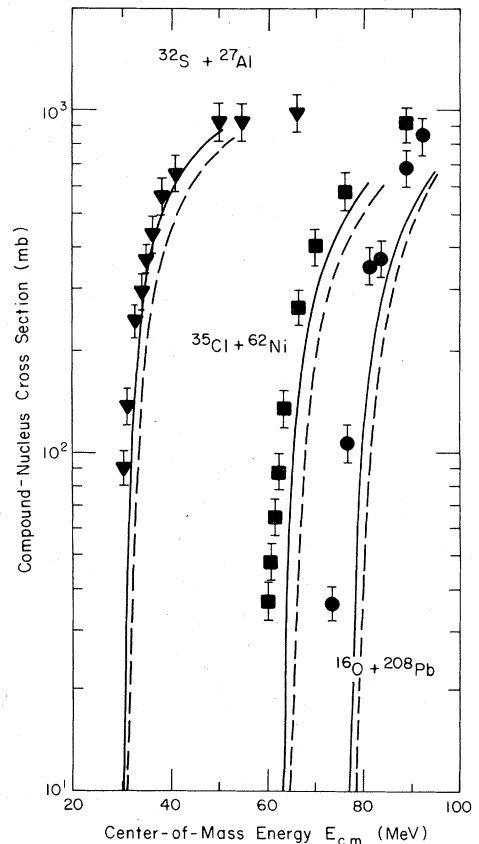


FIG. 9. Comparison of calculated and experimental compound-nucleus cross sections for three nuclear systems. The experimental points are taken from the following: \blacktriangledown from Refs. 68 and 69, \blacksquare from Refs. 60 and 68, and \bullet from Refs. 68 and 70. The solid curves are calculated with our standard Yukawa-plus-exponential potential, and the dashed curves are calculated with the proximity potential of Ref. 32.

quate. Either the formation of a neck through the dynamical deformation of the target and projectile,⁷¹ or the presence of zero-point vibrations in the target and projectile,⁷² could increase the penetrability relative to that calculated for a one-dimensional barrier.

The discrepancies shown in Fig. 9 would be even larger if there is a dissipation of energy in the entrance channel. However, if this is accompanied by the transfer of orbital angular momentum into the spin of the two nuclei, then the calculated cross section will be affected in the opposite direction.⁷³ The discrepancy would also be larger if highly inelastic processes compete with the formation of compound nuclei.

We also show by the dashed lines in Fig. 9 the results calculated with the proximity potential.³² The larger discrepancies for this potential arise because the barriers calculated with the proximity potential are higher than those calculated with the Yukawa-plus-exponential potential.

V. FISSION

We turn now to nuclear fission, which probes the nuclear potential energy of deformation for shapes that are more compact than those in heavy-ion reactions. In fission, the macroscopic potential energy is often calculated by means of the liquid-drop model⁹ or the droplet model,¹⁰⁻¹² which neglect the finite range of the nuclear force and the diffuse nuclear surface. As seen with the original single-Yukawa model,¹⁹⁻²³ these effects strongly influence the variation throughout the Periodic Table of the fission saddle-point energy and shape. In this section we calculate these quantities with our new Yukawa-plus-exponential model and compare some of the results with those of the three previous models^{9-12, 19-23} and with experimental data.

For nuclei along Green's approximation to the line of β stability,⁷⁴ we compare in Fig. 10 fission-barrier heights calculated with these four different macroscopic models. The barrier heights in the droplet model are calculated for γ -family shapes,⁷⁵ whereas those in the other three models are calculated by varying all three symmetric deformation coordinates in the three-quadratic-surface shape parametrization.⁷⁶ Standard methods are used for calculating the Coulomb energy.⁷⁷

The two models that include the finite range of the nuclear force and the diffuse nuclear surface yield results that are very similar to each other, although for all nuclei the barriers calculated with the new Yukawa-plus-exponential model are slightly higher than those calculated with the orig-

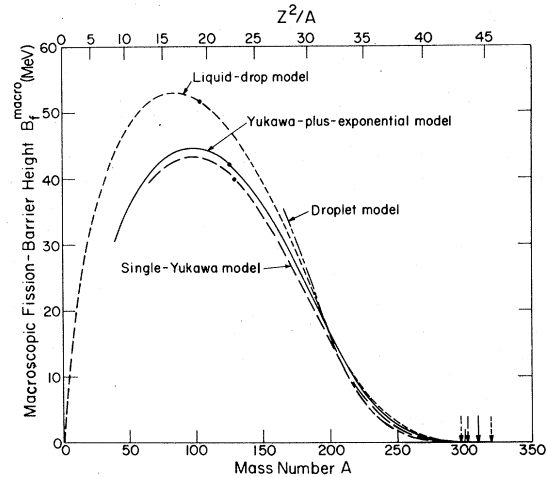


FIG. 10. Comparison of macroscopic fission-barrier heights calculated for nuclei along the line of β stability with four different models. The constants used in the liquid-drop model, droplet model, and single-Yukawa model are the original values given in Refs. 9, 11, 12, and 19. The solid circles indicate for three of the models the Businaro-Gallone point, where stability of the saddle-point shape against mass-asymmetric distortions is lost. The arrows along the abscissa indicate for each model the point at which the system loses stability against fission.

inal single-Yukawa model. The results of these two models are different from those of either the liquid-drop model or the droplet model, except for nuclei with mass number $A \approx 200$, where the barrier heights calculated with the four models are approximately equal. For heavier nuclei, the droplet model yields the lowest barrier and the liquid-drop model yields the highest, with the other two models yielding results that are intermediate. For lighter nuclei, barriers calculated in the droplet model are highest and those calculated in the liquid-drop model are second highest, with those calculated in the other two models lying somewhat lower.

The solid points in Fig. 10 indicate for three of the models the critical Businaro-Gallone point, at which stability of the saddle-point shape against mass-asymmetric deformations is lost.⁷⁸ This critical point is shifted to heavier nuclei in the Yukawa-plus-exponential model and single-Yukawa model, compared to the liquid-drop model.

To illustrate the effect of the finite range of the nuclear force and the diffuse nuclear surface on saddle-point shapes, we compare in Fig. 11 for nuclei along the line of β stability⁷⁴ the maximum and minimum radii of these shapes calculated in the Yukawa-plus-exponential model with those calculated in the liquid-drop model. In both models,

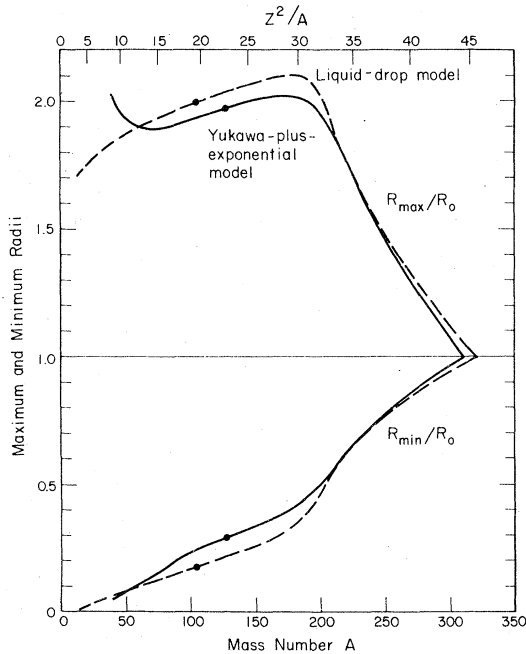


FIG. 11. Maximum and minimum radii of saddle-point shapes for nuclei along the line of β stability. The solid curves give the results calculated in our Yukawa-plus-exponential model, and the dashed curves give the results calculated in the liquid-drop model with the constants of Ref. 9. The solid circles indicate for each model the Businaro-Gallone point.

the saddle-point shapes undergo a qualitative transition⁷⁹ from cylinderlike shapes for $A \gtrsim 200$ to dumbbell-like shapes for $A \lesssim 200$. However, this transition is smoother in the Yukawa-plus-exponential model than in the liquid-drop model. For $A \gtrsim 60$ the dumbbell-like shapes are more compact in the Yukawa-plus-exponential model than in the liquid-drop model, whereas for $A \lesssim 60$ the converse is true.

The results shown in Figs. 10 and 11 are influenced both by intrinsic differences in the models themselves and by differences in the values of the constants that are used. For example, the surface-asymmetry constant κ_s has the value 1.7826 in the liquid-drop model,⁹ 3.0 in the Yukawa-plus-exponential model, and 4.0 in the single-Yukawa model.¹⁹ This means that as we move from heavy nuclei to light nuclei, where the relative neutron-proton excess I is smaller, the effective surface-energy constant c_s given by Eq. (3) becomes relatively smaller for the liquid-drop model and larger for the single-Yukawa model, compared to that for the Yukawa-plus-exponential model. In addition, the nuclear-radius constant r_0 has the value 1.2249 fm in the liquid-drop model, 1.18

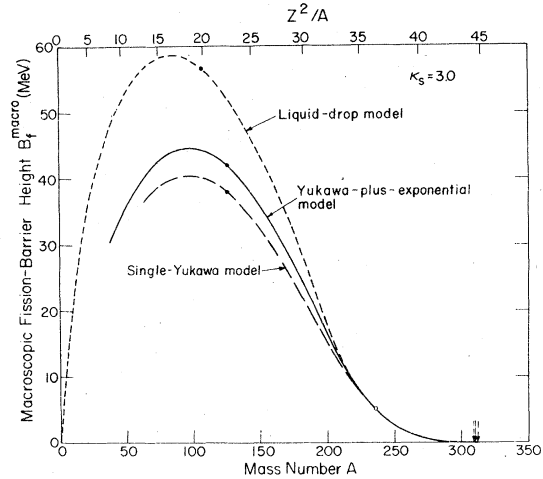


FIG. 12. Comparison of macroscopic fission-barrier heights calculated for nuclei along the line of β stability with three different models. We use a common value of $\kappa_s = 3.0$ for the surface-asymmetry constant and a common value of $r_0 = 1.18$ fm for the nuclear-radius constant, but retain the original values of the range a that were used for each model. The surface-energy constant a_s is adjusted in the liquid-drop model and the single-Yukawa model to yield the same fission-barrier height for ^{236}U as in the Yukawa-plus-exponential model; this common point is indicated by the open circle. For each model the solid circles indicate the Businaro-Gallone point, and the arrows along the abscissa indicate the point at which the system loses stability against fission.

fm in the Yukawa-plus-exponential model, and 1.16 fm in the single-Yukawa model.

To remove some of the trivial effects caused by differences in the values of the constants, we also calculate fission barriers for common values of $\kappa_s = 3.0$ and $r_0 = 1.18$ fm, with the surface-energy constant a_s adjusted to yield for ^{236}U the same barrier height as in the Yukawa-plus-exponential model. The range a of the folding function in each case remains unchanged from its previous value, which is zero for the liquid-drop model, 0.65 fm for the Yukawa-plus-exponential model, and 1.4 fm for the single-Yukawa model. The resulting values of a_s are 19.685 MeV for the liquid-drop model, 21.7 MeV for the Yukawa-plus-exponential model, and 23.05 MeV for the single-Yukawa model. As shown in Fig. 12, the barriers calculated in this way for light nuclei are somewhat higher in the liquid-drop model and somewhat lower in the single-Yukawa model compared to the corresponding results in Fig. 10.

In Fig. 13 we compare calculated and experimental macroscopic fission-barrier heights for nuclei ranging from ^{250}Cm down to ^{179}Ta . Because the barrier height is measured in units of

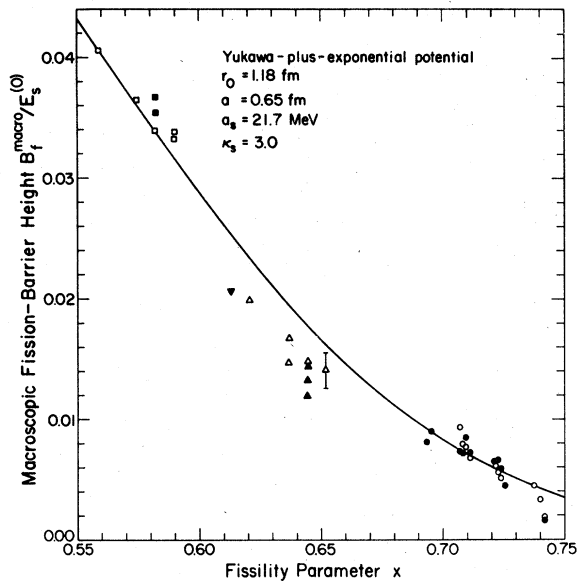


FIG. 13. Comparison of calculated and experimental macroscopic fission-barrier heights as a function of the fissility parameter x defined by Eq. (13). The circles give the experimental values for actinide nuclei (Refs. 47, 49, and 50), and the triangles and squares give those for lighter nuclei (Refs. 34, 48, and 49). Typical uncertainties in the experimental points are indicated by the error bar.

$E_s^{(0)}$ and the fissioning nucleus is specified in terms of the fissility parameter x [see Eqs. (9) and (13)], the curve calculated for nuclei along the line of β stability is also approximately correct for nuclei off the line of β stability. Similarly, when plotted in this way, the curve is also approximately correct for other values of a_s and κ_s , although it depends fairly sensitively upon a and r_0 , since these quantities affect the critical value of x at which the spherical shape loses stability against fission [see Eqs. (12) and (16)].

The circles in Fig. 13 give the experimental macroscopic contributions for actinide nuclei, derived from the experimental fission-barrier heights of Ref. 47 and the calculated fission barriers of Ref. 49. The solid circles represent values obtained from the second saddle point, and the open circles represent values obtained from the first saddle point, where the results of Ref. 50 have been used to correct for the lowering in energy due to axially asymmetric distortions. The remaining points for lighter nuclei are derived from the experimental fission-barrier heights of Ref. 48. The solid triangles and squares represent values for even nuclei, for which the calculated fission barriers of Ref. 49 have been used to extract the macroscopic con-

tributions. The open triangles and squares represent values for odd nuclei, for which the calculated ground-state single-particle corrections of Ref. 34 have been interpolated to correct for single-particle effects at the ground state only.

The systematic discrepancies that are evident for the triangles in Fig. 13 arise primarily from errors in the calculated ground-state single-particle corrections for nuclei near the doubly magic nucleus ^{208}Pb . The agreement between these points and the curve would be improved significantly if we were to replace our calculated ground-state single-particle corrections by experimental values, as is customarily done in comparisons of this type.^{9, 11, 12, 48}

Although the experimental determination of fission-barrier heights for light nuclei with $A \approx 100$ is very difficult, three recent studies indicate that the barriers for such nuclei are somewhat lower than those calculated in the liquid-drop model.⁸⁰⁻⁸² Taken together with our present calculations, these results suggest that the finite range of the nuclear force and the diffuse nuclear surface are lowering the barriers for light nuclei relative to those calculated in the liquid-drop model and droplet model.

VI. GROUND-STATE MASSES AND DEFORMATIONS

Our final application of the Yukawa-plus-exponential model is to nuclear ground-state masses and deformations. At this stage of our work, we calculate the single-particle correction that is added to Eq. (25) in two separate ways.

In the first way, we use the folded-Yukawa-II single-particle potential, whose parameters were adjusted to reproduce experimental single-particle levels in deformed actinide nuclei.³⁴ With shell and pairing corrections calculated from this potential by use of Strutinsky's method,⁶⁻⁸ and with the deformation dependence of the macroscopic energy calculated from the droplet model,¹⁰⁻¹² single-particle corrections have been calculated previously for even deformed actinide nuclei.³⁴ We also use this potential to calculate the single-particle corrections for even spherical nuclei in four regions of the Periodic Table, where the deformation dependence of the energy does not enter. In this way a total of 165 even nuclei are considered.

In the second way, we calculate single-particle corrections by use of the method of Myers and Swiatecki.^{9, 11, 12} In determining the ground-state shape and energy, we treat the Coulomb energy and generalized surface energy to second order in the quadrupole deformation coordinate, for which

purpose Eqs. (10) and (12) prove useful. In this way a total of 1340 nuclei are considered.

For various sets of constants, the root-mean-square errors in the masses calculated the first way are shown in Table II, and those calculated the second way are shown in Table III. In each case the range a of the Yukawa-plus-exponential potential is set equal to 0.65 fm, and the nuclear-radius constant r_0 and the Wigner constant W are set equal to the indicated values.

With $W=30$ MeV, which is the value determined by Myers from an examination of the masses of light nuclei near the $N=Z$ line,^{11, 12} the first five rows of each table show the dependence of the results upon r_0 , when all four of the remaining constants are varied to minimize the root-mean-square error in the calculated masses. With both of the single-particle corrections that we have used, ground-state masses prefer the value of r_0 to be somewhat less than 1.16 fm.

With $r_0=1.18$ fm, the next three rows of each table show the dependence of the results upon W , when all four of the remaining constants are varied in the least-squares minimization. At this value of r_0 , ground-state masses prefer the value of W to be somewhat larger than 40 MeV.

With $r_0=1.18$ fm and $W=30$ MeV, the next three

rows of each table show the dependence of the results upon κ_s , when the remaining three constants a_s , κ_v , and a_v are varied. At these values of r_0 and W , the ground-state masses of 165 even nuclei calculated the first way prefer the value of κ_s to be about 2.8, whereas the ground-state masses of 1340 nuclei calculated the second way prefer the value of κ_s to be about 3.2, which confirms that the value of κ_s is determined very poorly.

With $r_0=1.18$ fm, $W=30$ MeV, and $\kappa_s=3.0$, the last four rows of each table show the dependence of the results upon a_s , when the remaining two constants κ_v and a_v are varied. At these values of r_0 , W , and κ_s , ground-state masses prefer the value of a_s to be slightly larger than the value of 21.7 MeV determined from fission-barrier heights. As can be seen from Eq. (28) and Fig. 3, this discrepancy could be removed by increasing somewhat the value of either W or r_0 .

In Fig. 14 we show the experimental and calculated single-particle corrections, as well as their differences, corresponding to the set of constants given by Eqs. (29), which is the set listed in row 13 of Table II for the folded-Yukawa-II single-particle potential. Some of the discrepancies evident in this figure for the lighter actinide nuclei arise because the droplet model, which is

TABLE II. Root-mean-square error in the calculated ground-state masses of 165 even nuclei in the actinide region and four regions of spherical nuclei, for various sets of constants. Single-particle corrections are calculated from the folded-Yukawa-II single-particle potential (Ref. 34), with a constant zero-point energy of 0.5 MeV used for each nucleus. The range a of the Yukawa-plus-exponential potential is set equal to 0.65 fm. Constants to the left of the dashed line are held fixed at the indicated values, whereas those to the right of the dashed line are varied in the least-squares minimization.

r_0 (fm)	W (MeV)	κ_s	a_s (MeV)	κ_v	a_v (MeV)	Error (MeV)
1.16	30	2.52	22.485	1.96	16.216	0.96
1.17	30	2.64	22.150	1.98	16.127	0.97
1.18	30	2.77	21.823	2.00	16.040	1.00
1.19	30	2.90	21.504	2.02	15.955	1.04
1.20	30	3.04	21.193	2.04	15.871	1.09
1.18	0	2.16	21.993	1.89	16.055	1.11
1.18	20	2.57	21.880	1.96	16.045	1.01
1.18	40	2.98	21.766	2.04	16.035	1.00
1.18	30	2.8	21.840	2.01	16.043	1.00
1.18	30	3.0	21.969	2.06	16.066	1.02
1.18	30	3.2	22.097	2.10	16.089	1.09
1.18	30	3.0	21.6	2.03	15.993	1.26
1.18	30	3.0	21.7	2.04	16.012	1.15
1.18	30	3.0	21.8	2.05	16.032	1.08
1.18	30	3.0	21.9	2.05	16.052	1.03

TABLE III. Root-mean-square error in the calculated ground-state masses of 1340 nuclei with $Z \geq 6$, $N \geq 6$, and experimental error < 1 MeV, for various sets of constants. Single-particle corrections are calculated by use of the method of Myers and Swiatecki (Refs. 9, 11, and 12), without the addition of any zero-point energy. The range a of the Yukawa-plus-exponential potential is set equal to 0.65 fm. Constants to the left of the dashed line are held fixed at the indicated values, whereas those to the right of the dashed line are varied in the least-squares minimization.

r_0 (fm)	W (MeV)	κ_s	a_s (MeV)	κ_v	a_v (MeV)	Error (MeV)
1.16	30	3.00	23.055	2.08	16.323	1.71
1.17	30	3.12	22.738	2.11	16.240	1.78
1.18	30	3.24	22.430	2.13	16.158	1.85
1.19	30	3.36	22.129	2.15	16.078	1.93
1.20	30	3.48	21.836	2.17	16.000	2.02
1.18	0	2.56	22.689	2.01	16.193	2.29
1.18	20	3.01	22.516	2.09	16.170	1.99
1.18	40	3.47	22.343	2.17	16.146	1.73
1.18	30	2.8	22.177	2.02	16.111	1.91
1.18	30	3.0	22.293	2.07	16.133	1.87
1.18	30	3.2	22.409	2.12	16.154	1.85
1.18	30	3.0	21.6	2.02	15.984	2.29
1.18	30	3.0	21.7	2.03	16.006	2.19
1.18	30	3.0	21.8	2.03	16.027	2.09
1.18	30	3.0	21.9	2.04	16.049	2.01

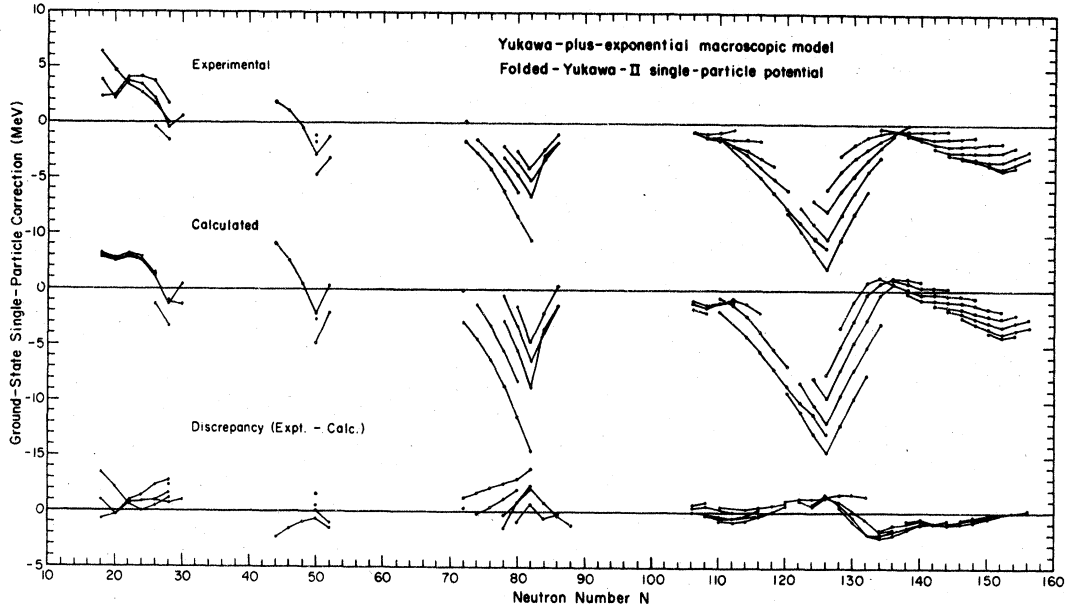


FIG. 14. Comparison of experimental and calculated ground-state single-particle corrections for even deformed actinide nuclei and for even spherical nuclei in four regions of the Periodic Table. The experimental correction is the difference between the measured ground-state mass of a nucleus (Ref. 35) and the value calculated for a spherical shape with Eq. (25). The calculated correction is the sum of the shell and pairing corrections calculated with the folded-Yukawa-II single-particle potential, whose parameters were adjusted to reproduce experimental levels in deformed actinide nuclei (Ref. 34).

relatively stiff with respect to hexadecapole deformations, was used to calculate the deformation dependence of the macroscopic energy. Other discrepancies arise because of deficiencies in the single-particle correction itself, particularly around closed-shell nuclei.

VII. LIMITATIONS

In summary, we have presented a new Yukawa-plus-exponential model for calculating the generalized nuclear surface energy, obtained by requiring that two semi-infinite slabs of constant-density nuclear matter have minimum energy at zero separation. The resulting unified nuclear potential reproduces experimental data for heavy-ion elastic scattering, fusion, fission, and ground-state masses. However, the model does have some specific limitations, and we would like to conclude with some general comments concerning the range of its applicability.

First of all, we stress that the form of our generalized surface energy does not imply that the nuclear surface is sharp. The equivalent sharp surface is introduced only as a reference surface in order to define the nuclear shape unambiguously. However, we do assume that the density profile perpendicular to the surface is the same at

all points on the surface, independent of the nuclear size and shape. This implies that our heavy-ion interaction potential (17) is based on the frozen-density approximation,³² since the possible polarization of the surface areas of the two nuclei is not taken into account. As Randrup has shown for two semi-infinite slabs of nuclear matter, such an effect is energetically favorable beginning at the relatively large distance $s \approx 3.44$ fm between their half-density points.⁶³ Because his calculation is purely static and because we do not know the time scale for polarization, we cannot check at this time the appropriateness of the frozen-density approximation. However, it is more likely to be valid for elastic scattering in the strong-absorption case than for fusion and elastic scattering with orbiting, where the interaction potential is probed at shorter distances between the nuclear surfaces.

The inherent limitation of our model to situations in which the density profile can be assumed to be frozen excludes a discussion of the neck rupture in fission. When a nucleus is close to its scission point, the central density in the neck is presumably smaller than the saturation density of the standard profile. Such a configuration is therefore excluded from consideration in our model. This can also be inferred formally from the lack of any information

about the nuclear compressibility in our model. A treatment of the neck rupture obviously requires some input information concerning the response of the neck region to external stress.

Surface tension arises physically because particles at the surface interact with a smaller number of surrounding particles than do particles in the interior. However, because the double volume integral (7) does not contribute to the energy in the interior, the surface energy in our model is produced by a delicate balance in Eq. (7) between the long-range attraction for distances $\sigma > 2a$ and the short-range repulsion for distances $\sigma < 2a$. This has the seemingly unphysical consequence that a nucleus would gain energy by decaying, for example, into two hemispheres, separated by a distance of order a between their newly created equivalent sharp surfaces. However, the actual density distribution corresponding to such a configuration would contain only a small depression along the internal crack. Such configurations with an internal density depression are excluded from consideration in our model because they violate the implicit assumption that the density is constant in the interior. An appropriate treatment of such a decay degree of freedom would require that the volume-energy term be density dependent, which would stabilize the system against granulation.

The incorporation of such a density dependence would represent a useful extension of our model.

However, even apart from that, there are several important refinements that should be studied within the present version of the Yukawa-plus-exponential model. It should be used to calculate heavy-ion elastic and inelastic scattering, nucleon-transfer reactions, and compound-nucleus formation for nuclear systems throughout the Periodic Table. In conjunction with an appropriate single-particle potential, it should be used to calculate fission barriers and ground-state masses and deformations for nuclei throughout the Periodic Table. Finally, it should be used in dynamical calculations of large-scale nuclear collective motion to study the descent of nuclei from their fission saddle points, as well as the fusion of colliding targets and projectiles. We hope that in the coming years our unified potential will prove useful in studies of this type.

ACKNOWLEDGMENTS

We are grateful to R. M. DeVries for permitting us to use his version of the program GENOA to calculate the elastic-scattering angular distributions in Fig. 8, and to J. M. Alexander, M. Blann, R. M. DeVries, J. R. Huizenga, G. R. Satchler, and W. J. Swiatecki for stimulating discussions concerning our new potential. This work was supported by the U. S. Department of Energy.

- ¹S. E. Koonin, K. T. R. Davies, V. Maruhn-Rezwani, H. Feldmeier, S. J. Krieger, and J. W. Negele, *Phys. Rev. C* **15**, 1359 (1977).
- ²J. W. Negele, S. E. Koonin, P. Möller, J. R. Nix, and A. J. Sierk, *Phys. Rev. C* **17**, 1098 (1978).
- ³C. Y. Wong and H. H. K. Tang, *Phys. Rev. Lett.* **40**, 1070 (1978).
- ⁴C. M. Shakin and M. S. Weiss, Lawrence Livermore Laboratory Report No. UCRL-80500, 1977 (unpublished).
- ⁵H. Orland and R. Schaeffer, C. E. N. Saclay Report No. DPh-T/78/41, 1978 (unpublished).
- ⁶M. Brack, J. Damgaard, A. S. Jensen, H. C. Pauli, V. M. Strutinsky, and C. Y. Wong, *Rev. Mod. Phys.* **44**, 320 (1972).
- ⁷S. G. Nilsson and J. Damgaard, *Phys. Scr.* **6**, 81 (1972).
- ⁸J. R. Nix, *Annu. Rev. Nucl. Sci.* **22**, 65 (1972).
- ⁹W. D. Myers and W. J. Swiatecki, *Ark. Fys.* **36**, 343 (1967).
- ¹⁰W. D. Myers and W. J. Swiatecki, *Ann. Phys. (N.Y.)* **55**, 395 (1969).
- ¹¹W. D. Myers, *At. Data Nucl. Data Tables* **17**, 411 (1976).
- ¹²W. D. Myers, *Droplet Model of Atomic Nuclei* (IFI/Plenum, New York, 1977).
- ¹³H. A. Bethe, *Phys. Rev.* **167**, 879 (1968).
- ¹⁴R. A. Berg and L. Willets, *Phys. Rev.* **101**, 201 (1956).
- ¹⁵K. A. Brueckner, J. R. Buchler, S. Jorna, and R. J. Lombard, *Phys. Rev.* **171**, 1188 (1968).
- ¹⁶R. J. Lombard, *Ann. Phys. (N.Y.)* **77**, 380 (1973).
- ¹⁷C. Ngô, B. Tamain, J. Galin, M. Beiner, and R. J. Lombard, *Nucl. Phys.* **A240**, 353 (1975).
- ¹⁸W. Scheid and W. Greiner, *Z. Phys.* **226**, 364 (1969).
- ¹⁹H. J. Krappe and J. R. Nix, in *Proceedings of the Third International Atomic Energy Agency Symposium on the Physics and Chemistry of Fission, Rochester, New York, 1973* (International Atomic Energy Agency, Vienna, 1974), Vol. I, p. 159.
- ²⁰J. R. Nix and A. J. Sierk, *Phys. Scr.* **10A**, 94 (1974).
- ²¹P. Möller and J. R. Nix, *Nucl. Phys.* **A272**, 502 (1976).
- ²²P. Möller and J. R. Nix, *Nucl. Phys.* **A281**, 354 (1977).
- ²³H. J. Krappe, *Nucl. Phys.* **A269**, 493 (1976).
- ²⁴P. G. Zint and U. Mosel, *Phys. Rev. C* **14**, 1488 (1976).
- ²⁵A. J. Sierk, in *Proceedings of the Symposium on Heavy-Ion Elastic Scattering, Rochester, New York, 1977* [University of Rochester report, 1977 (unpublished)], p. 306.
- ²⁶G. R. Satchler and W. G. Love, *Phys. Lett.* **65B**, 415 (1976).
- ²⁷H. J. Krappe, J. R. Nix, and A. J. Sierk, *Phys. Rev.*

- Lett. 42, 215 (1979).
- ²⁸K. T. R. Davies and J. R. Nix, Phys. C 14, 1977 (1976).
- ²⁹A. R. Edmonds, *Angular Momentum in Quantum Mechanics* (Princeton University Press, Princeton, 1960), 2nd edition.
- ³⁰*Handbook of Mathematical Functions*, edited by M. Abramowitz and I. A. Stegun (National Bureau of Standards, Washington, D. C., 1964), pp. 437-441.
- ³¹N. Bohr and J. A. Wheeler, Phys. Rev. 56, 426 (1939).
- ³²J. Błocki, J. Randrup, W. J. Swiatecki, and C. F. Tsang, Ann. Phys. (N.Y.) 105, 427 (1977).
- ³³H. A. Bethe and R. F. Bacher, Rev. Mod. Phys. 8, 82 (1936).
- ³⁴P. Möller, S. G. Nilsson, and J. R. Nix, Nucl. Phys. A229, 292 (1974).
- ³⁵A. H. Wapstra and K. Bos, At. Data Nucl. Data Tables 19, 175 (1977).
- ³⁶T. G. Trippe, A. Barbaro-Galtieri, R. L. Kelly, A. Rittenberg, A. H. Rosenfeld, G. P. Yost, N. Barash-Schmidt, C. Bricman, R. J. Hemingway, M. J. Losty, M. Roos, V. Chaloupka, and B. Armstrong, Rev. Mod. Phys. 48, S1 (1976).
- ³⁷C. W. de Jager, H. de Vries, and C. de Vries, At. Data Nucl. Data Tables 14, 479 (1974).
- ³⁸W. D. Myers, Nucl. Phys. A204, 465 (1973).
- ³⁹G. R. Satchler, in *Proceedings of the International Conference on Reactions between Complex Nuclei, Nashville, Tennessee, 1974* (North-Holland, Amsterdam/American Elsevier, New York, 1974), Vol. 2, p. 171.
- ⁴⁰G. R. Satchler, in *Proceedings of the INS International Symposium on Nuclear Direct Reaction Mechanisms, Fukuoka, Japan, 1978* (to be published).
- ⁴¹G. R. Satchler, in *Proceedings of the Sixth INS Summer School on Nuclear Physics, Dogashima, Japan, 1978* (unpublished).
- ⁴²G. R. Satchler and W. G. Love, Oak Ridge National Laboratory report, 1979 (unpublished).
- ⁴³Y. Eisen and Z. Vager, Nucl. Phys. A187, 219 (1972).
- ⁴⁴P. R. Christensen and Z. E. Switkowski, Nucl. Phys. A280, 205 (1977).
- ⁴⁵J. Borysowicz and J. H. Hetherington, Phys. Rev. C 7, 2293 (1973).
- ⁴⁶J. L. Friar and J. W. Negele, Adv. Nucl. Phys. 8, 219 (1975).
- ⁴⁷B. B. Back, O. Hansen, H. C. Britt, and J. D. Garrett, Phys. Rev. C 9, 1924 (1974).
- ⁴⁸L. G. Moretto, S. G. Thompson, J. Routti, and R. C. Gatti, Phys. Lett. 38B, 471 (1972).
- ⁴⁹P. Möller and J. R. Nix, Nucl. Phys. A229, 269 (1974).
- ⁵⁰S. E. Larsson, Phys. Scr. 8, 17 (1973).
- ⁵¹H. Feshbach, Ann. Phys. (N.Y.) 19, 287 (1962).
- ⁵²H. J. Krappe, Ann. Phys. (N.Y.) 99, 142 (1976).
- ⁵³D. A. Goldberg, S. M. Smith, and G. F. Burdzik, Phys. Rev. C 10, 1362 (1974).
- ⁵⁴J. G. Cramer, R. M. DeVries, D. A. Goldberg, M. S. Zisman, and C. F. Maguire, Phys. Rev. C 14, 2158 (1976).
- ⁵⁵R. Vandenbosch, M. P. Webb, T. D. Thomas, S. W. Yates, and A. M. Friedman, Phys. Rev. C 13, 1893 (1976).
- ⁵⁶P. R. Christensen and A. Winther, Phys. Lett. 65B, 19 (1976).
- ⁵⁷J. B. Ball, C. B. Fulmer, E. E. Gross, M. L. Halbert, D. C. Hensley, C. A. Ludemann, M. J. Saltmarsh, and G. R. Satchler, Nucl. Phys. A252, 208 (1975).
- ⁵⁸S. E. Vigdor, D. G. Kovar, P. Sperr, J. Mahoney, A. Menchaca-Rocha, C. Olmer, and M. Zisman, Bull. Am. Phys. Soc. 23, 615 (1978).
- ⁵⁹J. R. Birkelund and J. R. Huizenga, Phys. Rev. C 17, 126 (1978).
- ⁶⁰W. Scobel, H. H. Gutbrod, M. Blann, and A. Mignerey, Phys. Rev. C 14, 1808 (1976).
- ⁶¹P. David, J. Bisplinghoff, M. Blann, T. Mayer-Kuckuk, and A. Mignerey, Nucl. Phys. A287, 179 (1977).
- ⁶²R. M. DeVries (private communication).
- ⁶³F. Perey (unpublished).
- ⁶⁴P. Braun-Munzinger, G. M. Berkowitz, T. M. Cormier, C. M. Jachcinski, J. W. Harris, J. Barrette, and M. J. LeVine, Phys. Rev. Lett. 38, 944 (1977).
- ⁶⁵R. M. DeVries, D. A. Goldberg, J. W. Watson, M. S. Zisman, and J. G. Cramer, Phys. Rev. Lett. 39, 450 (1977).
- ⁶⁶D. L. Hill and J. A. Wheeler, Phys. Rev. 89, 1102 (1953).
- ⁶⁷H. J. Krappe, in *Proceedings of the International Workshop VI on Gross Properties of Nuclei and Nuclear Excitations, Hirscheegg, Kleinwalsertal, Austria, 1978* [Technische Hochschule Darmstadt Report No. AED-Conf-78-007-001-AED-Conf-78-007-041, 1978 (unpublished)], p. 52.
- ⁶⁸L. C. Vaz and J. M. Alexander, Phys. Rev. C 18, 2152 (1978).
- ⁶⁹H. H. Gutbrod, W. G. Winn, and M. Blann, Nucl. Phys. A213, 267 (1973).
- ⁷⁰F. Videbaek, R. B. Goldstein, L. Grodzins, S. G. Steadman, T. A. Belote, and J. D. Garrett, Phys. Rev. C 15, 954 (1977).
- ⁷¹H. Holm and W. Greiner, Phys. Rev. Lett. 24, 404 (1970).
- ⁷²T. Kodama, R. A. M. S. Nazareth, P. Möller, and J. R. Nix, Phys. Rev. C 17, 111 (1978).
- ⁷³J. R. Birkelund, J. R. Huizenga, J. N. De, and D. Sperber, Phys. Rev. Lett. 40, 1123 (1978).
- ⁷⁴A. E. S. Green, *Nuclear Physics* (McGraw-Hill, New York, 1955), pp. 185, 250.
- ⁷⁵M. Bolsterli, E. O. Fiset, J. R. Nix, and J. L. Norton, Phys. Rev. C 5, 1050 (1972).
- ⁷⁶J. R. Nix, Nucl. Phys. A130, 241 (1969).
- ⁷⁷K. T. R. Davies and A. J. Sierk, J. Comp. Phys. 18, 311 (1975).
- ⁷⁸U. L. Businaro and S. Gallone, Nuovo Cimento 5, 315 (1957).
- ⁷⁹S. Cohen and W. J. Swiatecki, Ann. Phys. (N.Y.) 22, 406 (1963).
- ⁸⁰N. C. Mukhopadhyay, J. Hadermann, and K. Junker, Nucl. Phys. (to be published).
- ⁸¹A. S. Iljinov, E. A. Cherepanov, and S. E. Chigrinov (unpublished).
- ⁸²B. Schröder (unpublished).
- ⁸³J. Randrup, in *Nuclear Chemistry Annual Report, 1973* [Lawrence Berkeley Laboratory Report No. LBL-2366, 1974 (unpublished)], p. 137.